

Far-UV and Optical Emissions from Three Very Large Supernova Remnants Located at Unusually High Galactic Latitudes

Robert A. Fesen 6, Marcel Drechsler Kathryn E. Weil 6, Xavier Strottner 4, John C. Raymond 5, Justin Rupert 6,

Dan Milisavljevic 6, Bhagya M. Subrayan 6, Dennis di Cicco 7, Sean Walker 6, David Mittelman 7, and Mathew Ludgate 8

1 6127 Wilder Lab, Department of Physics and Astronomy, Dartmouth College, Hanover, NH 03755, USA

2 Sternwarte Bärenstein, Feldstraße 17, D-09471 Bärenstein, Germany

3 Department of Physics and Astronomy, Purdue University, 525 Northwestern Avenue, West Lafayette, IN 47907, USA

4 Montfraze, F-01370 Saint Etienne Du Bois, France

5 Harvard-Smithsonian Center for Astrophysics, 60 Garden St., Cambridge, MA 02138, USA

6 MDM Observatory, Kitt Peak National Observatory, 950 N. Cherry Ave., Tucson, AZ 85719, USA

7 MDW Sky Survey, New Mexico Skies Observatory, Mayhill, NM 88339, USA

8 Ross Creek Observatory, Dunedin 9010, New Zealand

Received 2021 February 24; revised 2021 June 10; accepted 2021 June 11; published 2021 October 20

Abstract

Galactic supernova remnants (SNRs) with angular dimensions greater than a few degrees are relatively rare, as are remnants located more than 10° off the Galactic plane. Here we report a UV and optical investigation of two previously suspected SNRs more than 10° in both angular diameter and Galactic latitude. One is a proposed remnant discovered in 2008 through 1420 MHz polarization maps near Galactic coordinates $l=353^{\circ}$, $b=-34^{\circ}$. GALEX far-UV (FUV) and H α emission mosaics show the object's radio emission coincident with an $11^{\circ} \times 14^{\circ}$ shell of UV filaments that surrounds a diffuse H α emission ring. Another proposed high-latitude SNR is the $20^{\circ} \times 26^{\circ}$ Antlia nebula (G275.5+18.4) discovered in 2002 through low-resolution all-sky H α and ROSAT soft X-ray emissions. GALEX FUV and H α mosaics along with optical spectra indicate the presence of shocks throughout the Antlia nebula with estimated shock velocities of 70 to over $100 \, \mathrm{km \ s^{-1}}$. We also present evidence that it has collided with the NE rim of the Gum Nebula. We find both of these large nebulae are bona fide SNRs with ages less than $10^{5} \, \mathrm{yr}$ despite their unusually large angular dimensions. We also present FUV and optical images along with optical spectra of a new high-latitude SNR (G249.7+24.7) some 4.5° in diameter which has also been independently discovered in X-rays and radio (Becker at al. 2021). We find this remnant's distance to be $\leqslant 400 \, \mathrm{pc}$ based on the detection of red and blue Na I absorption features in the spectra of two background stars.

Unified Astronomy Thesaurus concepts: Supernova remnants (1667)

1. Introduction

In spite of an increasing variety of supernova (SN) subtypes, the majority of SNe are generally believed to release $(0.5-2) \times 10^{51}$ erg, although superluminous SNe may release substantially more (Howell 2017). Only a small percentage of this comes out as visible light, with most of an SN's energy is initially carried away in the form of kinetic energy. It is this enormous point deposition of energy that has a significant impact on the structure and energy content of a galaxy's interstellar medium through an expanding remnant that can last largely intact up to $\simeq 10^5$ yr (Cox & Smith 1974; McKee & Ostriker 1977; Shull et al. 1989; Blondin et al. 1998).

Currently, there are some 300 confirmed Galactic supernova remnants (SNRs) cataloged with dozens of other suspected SNRs and more added every few years (Ferrand & Safi-Harb 2012; Green 2019). Most Galactic SNRs are less than a degree in angular size, more than 1 kpc distant, and well evolved, with typical estimated ages between 10⁴ and 10⁵ yr.

Outsized attention relative to their population percentage has been directed to the handful of the Milky Way's young remnants with ages less than 5000 yr. These include the Crab Nebula, Cassiopeia A, the remnants of Tycho and Kepler, the Vela remnant, and Puppis A. This increased attention is due to their high expansion velocities, metal-rich ejecta, bright emission across the entire electromagnetic spectrum, and clearer connections to the various core-collapse and thermonuclear SN subtypes.

The majority of Galactic SNRs are first detected through radio observations due to their characteristic synchrotron nonthermal radio emission associated with shocked gas (Downes 1971; Chevalier 1977; Green 1984, 2004). Such nonthermal emission leads to a power-law flux density, S, with $S \propto \nu^{-\alpha}$, where α is the emission spectral index with typical SNR values between -0.3 and -0.7. Rarer pulsar wind-driven SNRs exhibit a much flatter radio spectrum, with spectral indices around zero.

While multifrequency radio surveys have been historically the dominant tool for finding SNRs, X-ray studies have also led to the discovery of several additional SNRs. These include RX J1713.7–3946 (G347.3–0.5; Pfeffermann & Aschenbach 1996) and the young "Vela Junior" SNR (G266.2–1.2; Aschenbach 1998) coincident with the much larger Vela SNR. Recent examples of X-ray-confirmed or -discovered remnants include several new SNRs in the LMC (Maggi et al. 2014) and X-ray confirmation of the suspected Galactic remnant G53.4+0.0 (Driessen et al. 2018).

Despite the fact that fewer than 50% of Galactic SNRs exhibit any appreciable associated optical emission, a remnant's optical emission can be useful in confirming the presence of high-velocity shocks and in defining a remnant's overall size and morphology. Although discoveries of new SNRs in the optical are relatively rare, there have been several recently reported discoveries (Stupar et al. 2007, 2018; Boumis et al. 2009; Stupar & Parker 2012; Fesen et al. 2015, 2019; Neustadt et al. 2017; How et al. 2018) along with many proposed SNR candidates (Stupar et al. 2008; Boumis et al. 2009; Stupar & Parker 2011; Alikakos et al. 2012; Sabin et al. 2013).

Table 1
Locations and Dimensions of SNRs

SNR ID	Galactic Coordinates	Approximate Center (J2000)	Angular Size	Estimated Distance
G249+24	$l = 249.7 \ b = +24.7$	R.A. = $09^{h}33^{m}$ decl. = $-17^{\circ}00'$	4°.5	<390 pc
Antlia	$l = 275.5 \ b = +18.4$	$R.A. = 10^{h}38^{m} decl. = -37^{\circ}20'$	$20^{\circ} \times 26^{\circ}$	\sim 250 pc
G354-33	$l = 354.0 \ b = -33.5$	R.A. = $20^{\rm h}16^{\rm m}$ decl. = $-45^{\circ}50'$	$11^{\circ} \times 14^{\circ}$	<400 pc

The main criterion for optical SNR identification is a line ratio of $I([S\,II])/I(H\alpha) \geqslant 0.4$, which has proven useful in identifying the shocked emission of SNRs in both the Milky Way and nearby Local Group galaxies (Blair et al. 1981; Dopita et al. 1984; Fesen et al. 1985; Leonidaki et al. 2013; Long 2017). Recently, the near-infrared [Fe II] line emissions at 1.27 and 1.64 μ m have also been used to detect dust-obscured SNRs in nearby galaxies (see review by Long 2017).

One wavelength regime that has not yet been fully exploited to search for new Galactic SNRs is the ultraviolet (UV). Here we present results of an initial study of SNRs located far away from the Galactic plane using wide field-of-view (FOV) UV images assembled from the Galaxy Evolution Explorer (GALEX) All-Sky survey (Bianchi 2009). We began this research by investigating two unusually high-latitude suspected SNRs including the exceptionally large Antlia remnant (McCullough et al. 2002) (see Table 1). During this work, we also found a new apparent SNR. However, after our initial submission, W. Becker kindly sent us a preprint of their independent discovery of this new remnant based on SRG/eRosita X-ray and Parks All-Sky Survey observations. Since their paper has now been published, we have cited their results in reference to our independent findings. UV and optical images plus some follow-up optical spectra are described in Section 2, with results presented in Section 3. We discuss the general properties of these SNRs in Section 4, with our conclusions and discussion of helpful follow-up observations given in Section 5.

2. Data and Observations

2.1. GALEX UV Images

The GALEX satellite was a NASA science mission led by the California Institute of Technology who operated it from 2003 July through 2012 February. The main instrument was a 50 cm diameter modified Ritchey–Chrétien telescope, a dichroic beam splitter and astigmatism corrector, and two microchannel plate detectors to simultaneously cover two wavelength bands with a 1°.25 FOC with a resolution of 1″.5 pixel $^{-1}$. Direct images were obtained in two broad bandpasses: a far-UV (FUV) channel sensitive to light in the 1344–1786 Å range, and a near-UV (NUV) channel covering 1771–2831 Å (Morrissey et al. 2007). The resulting images are circular in shape with an image FWHM resolution of $\sim\!\!4\rlap.{''}2$ and $\sim\!\!5\rlap.{''}3$ in the FUV and NUV bands, respectively.

Being mainly a mission to study the UV properties of galaxies in the local universe, GALEX survey images largely avoided the complex and external galaxy-poor Galactic plane. However, even its All-Sky Survey program focused away from the plane of the Milky Way did not cover all possible areas, leading to numerous gaps (see Figure 1). Nonetheless, some 26,000 square degrees were imaged to a depth of $m_{\rm AB} = 20.5$ (Bianchi 2009). Using the online GALEX images, large FUV and NUV image mosaics of several regions typically more than 10° off the Galactic plane were examined.

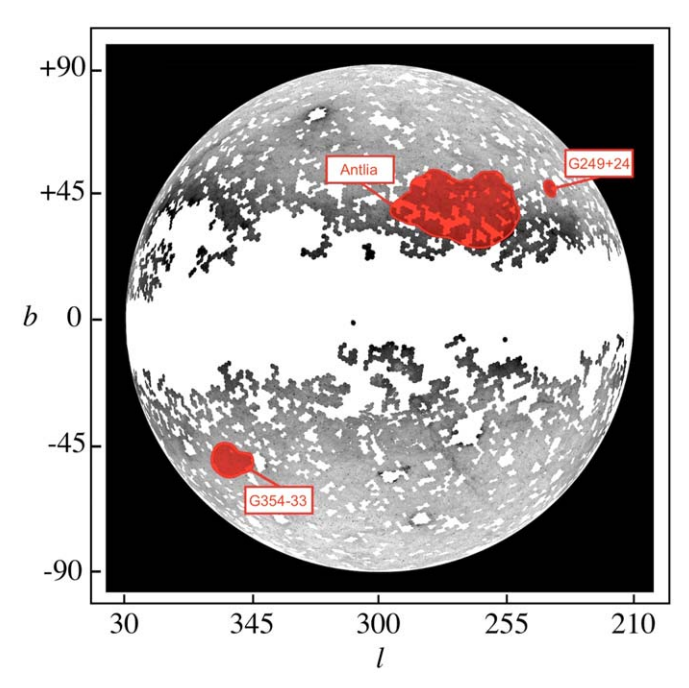


Figure 1. GALEX FUV intensity map of half of the sky in Galactic coordinates, showing locations of two apparent SNRs, G249+24 and G354-33, and the exceptionally large Antlia SNR. White areas denote regions with no GALEX imaging data.

2.2. Optical Images

Several different sources of narrow-passband optical images were used in our investigation of the three SNR candidates. Table 2 lists details of these optical images.

Wide-field, low-resolution $H\alpha$ images of regions around the suspected SNRs G249+24 and Antlia obtained as part of the MDW Hydrogen-Alpha Survey were used to provide general optical size and emission features. This survey uses a 130 mm f/2 camera at the New Mexico Skies Observatory, with an FLI ProLine 16803 CCD and a 3 nm filter centered on $H\alpha$. This telescope-camera system produced a field of view (FOV) of approximately 3°.5 × 3°.5 with a pixel size of 3″.17. Each field was observed 12 times each with an exposure of 1200 s.

We have also made large mosaics from Southern H α Sky Survey Atlas (SHASSA; Gaustad et al. 2001). This wide-angle robotic survey covered $\delta = +15^{\circ}$ to -90° with 13° square images with an angular resolution of $\simeq 0.4^{\circ}$. Narrow-passband continuum filters on the blue and red sides of H α centered at 6440 and 6770 Å allow for stellar and background subtraction. The survey had a native sensitive level of 1.2×10^{-17} erg cm⁻² s⁻¹ arcsec⁻², which could be significantly lowered with smoothing.

The western region of the Antlia remnant where it abuts the northeastern limb of the Gum Nebula was imaged using the H α + [N II], [O III], and [S II] filters using a 200 mm f/2 lens

https://www.mdwskysurvey.org

Table 2
Optical Data on SNRs

SNR	Survey or	Camera or	Direc	Spectra			
ID	Observatory	Telescope	Filters	FOV	Pixel Scale	Wavelength	FWHM
G249+24	MDW Hα Survey	130 mm lens	$H\alpha$	3°4 × 3°4	3."17	•••	
	MDM Observatory	2.4 m	$H\alpha + [NII]$	$18' \times 18'$	0."55	$\lambda 4000 - \lambda 6900$	3.5 Å
	MDM Observatory	2.4 m		•••	•••	$\lambda 5735 - \lambda 6065$	0.55 Å
Antlia	SHASSA Survey	f/1.6 52 mm lens	$H\alpha$, $\lambda 6440$, $\lambda 6770$	$13^{\circ} \times 13^{\circ}$	47."6		
	MDW H α Survey	130 mm lens	$_{ m Hlpha}$	3.4×3.4	3."17	•••	
	Ross Creek Obs.	$f/2.0\ 200\ {\rm mm\ lens}$	$\mathrm{H}\alpha + [\mathrm{N}\mathrm{II}], [\mathrm{O}\mathrm{III}], [\mathrm{S}\mathrm{II}]$	$10^{\circ}3 \times 6^{\circ}9$	3."87		
	SALT Observatory	10 m				$\lambda 4050 - \lambda 7120$	5.0 Å
G354-33	SHASSA Survey	f/1.6 52 mm lens	$H\alpha$, $\lambda 6440$, $\lambda 6770$	$13^{\circ} \times 13^{\circ}$	47."6	•••	
	CHILESCOPE	0.5 m	$\mathrm{H}\alpha$ + [N II], [O III]	1.1×1.1	0."96		

and a 9576 \times 6388 pixel ZWO ASI6200mm Pro CCD. This system provided an FOV of $10^{\circ}.3 \times 6^{\circ}.9$ with a $3.^{\prime\prime}.87$ pixel⁻¹ image scale. Total exposure times for the three filters listed above were 6.9 hr, 13.3 hr, and 6.8 hr respectively.

Higher-resolution images of the northwestern limb of the suspected G354–33 remnant were obtained with a 0.5 m Newtonian telescope at the CHILESCOPE Observatory located 25 km south of the Gemini South telescope in the Chilean Andes. A 4096 \times 4096 FLI PROLINE 16803 CCD camera was used that provided an FOV of 1°.1 \times 1°.1 with a pixel scale of 0."963 pixel⁻¹. Several 10 minute exposures were taken with H α + [N II] and [O III] filters.

Images of optical filaments detected in MDW images associated with GALEX FUV filaments in G249+24 were obtained with a 2.4 m telescope at the MDM Observatory at Kitt Peak, Arizona using the Ohio State Multi-Object Spectrograph (OSMOS; Martini et al. 2011) in direct imaging mode. With a 4096 \times 4096 CCD, this telescope/camera system yielded a clear FOV of $18^{\prime} \times 18^{\prime}$. With on-chip 2×2 or 4×4 pixel binning, spatial resolution was $0.^{\prime\prime}55$ and $1.^{\prime\prime}10$, respectively. Three exposures of 600-1200 s each using an $H\alpha+[N\,II]$ filter were taken at four positions where long-slit OSMOS spectra were also obtained (see below).

2.3. Optical Spectra

Low-dispersion optical spectra of filaments in the northern suspected SNR, G249+24, were obtained with the MDM 2.4 m Hiltner telescope using Ohio State Multi-Object Spectrograph (OSMOS; Martini et al. 2011). Employing a blue VPH grism (R=1600) and a 1."2 wide slit, exposures of 2 × 900 s were taken covering 4000–6900 Å with a spectral resolution of 1.2 Å pixel⁻¹ and an FWHM = 3.5 Å. Spectra were extracted from regions clean of appreciable emission along each of the 15' long slits.

As part of a program looking for high-velocity interstellar Na I absorption features in background stars in the direction of Galactic SNRs, moderate-dispersion spectra of over a dozen early-type stars with projected locations toward G249+24 and with estimated Gaia distances between 300 and 2000 pc were also observed on with the MDM 2.4 m Hiltner The data were taken using a Boller & Chivens Spectrograph (CCDS), which employs a Loral 1200×800 CCD detector. Using an 1800 groove mm⁻¹ grating blazed at 4700 Å yielded a wavelength coverage of 330 Å with a spectral scale of 0.275 Å per pixel. Exposure times varied from 1 to $2 \times 400 \, \text{s}$ to $3 \times 1200 \, \text{s}$ depending on star brightness and sky conditions.

A 1."3 wide slit was used, which resulted in a measured FWHM of 2.9 pixels, corresponding to a spectral resolution of 0.80 Å

providing an effective $R \simeq 7400$ at the Na I $\lambda\lambda 5890,5896$ lines. Although this spectral resolution is low compared to conventional interstellar absorption studies where R values typically equal or exceed 30,000, this spectrograph provided sufficient velocity resolution at the Na I lines for detecting $\geqslant 40~\rm km~s^{-1}$ interstellar absorption features seen in SNRs (Jenkins et al. 1976; Danks & Sembach 1995; Welsh & Sallmen 2003; Sallmen & Welsh 2004; Fesen et al. 2018; Ritchey 2020). Wavelength calibration was done using Hg and Ne comparison lamps and has been corrected to local standard of rest (LSR) values. Deblended absorption feature velocities are believed accurate to $\pm 4~\rm km~s^{-1}$.

For the southern hemisphere Antlia nebula, spectra were taken of suspected SNR filaments using the Robert Stobie Spectrograph (RSS) on the 10 m SALT telescope in South Africa. Using a 900 line per millimeter grating and a 1."5 wide slit, spectra were obtained covering the 4050–7120 Å region with an FWHM resolution of 5 Å and a dispersion of 1.0 Å pix⁻¹. Exposures ranged from $2 \times 300 \text{ s}$ to $2 \times 600 \text{ s}$.

MDM spectra were reduced using Pyraf software and OSMOS reduction pipelines¹⁰ in Astropy and PYRAF.¹¹ L. A. Cosmic (van Dokkum 2001) was used to remove cosmic rays and calibrated using a HgNe or Ar lamp and spectroscopic standard stars (Oke 1974; Massey & Gronwall 1990). SALT spectra were reduced using specific SALT reduction software.

3. Results

A few large and unusually high Galactic latitude nebulae have been recently proposed as previously unrecognized SNRs. These objects have angular diameters well in excess of the largest confirmed SNRs, such as the 8° diameter Vela SNR. If these objects were to be found to be true SNRs, they would expand the notion of how large an identifiable Galactic remnant can be and how far off the Galactic plane should SNR researchers be looking.

The proposed new SNRs include the huge $\sim 24^{\circ}$ diameter Antlia nebula (G275.5+18.4; McCullough et al. 2002) and the $\sim 10^{\circ}$ diameter radio remnant G354–33 (Testori et al. 2008). Due to limited data on it, Antlia is listed only as a possible SNR in the most recent catalog of Galactic SNRs (Green 2019), whereas no mention is made of G354–33 in either this 2019 SNR catalog or in online SNR lists. Below we discuss GALEX far-UV (FUV) and optical properties of these two suspected SNRs,

¹⁰ https://github.com/jrthorstensen/thorosmos

¹¹ PYRAF is a product of the Space Telescope Science Institute, which is operated by AURA for NASA.

¹² http://www.mrao.cam.ac.uk/surveys/snrs/snrs.info.html; http://snrcat.physics.umanitoba.ca/index.php?

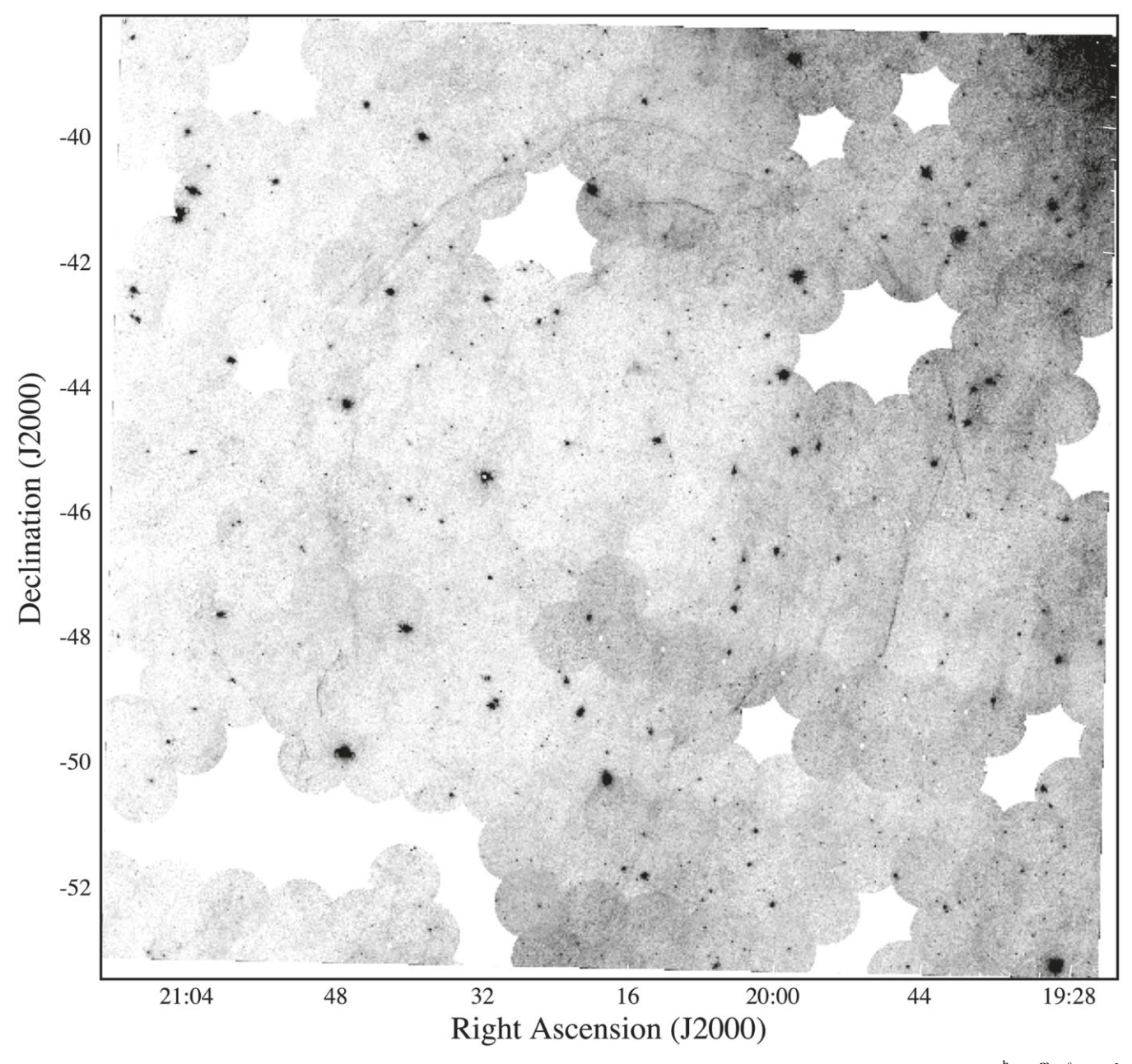


Figure 2. GALEX FUV intensity map of G354–33 showing a roughly spherical shell of UV emission filaments. Approximate shell center: 20^h16.0^m36^s, -45°40′. Note: Individual circular GALEX images are 1.°2 in diameter.

plus a third object, G249.2+24.4, which appears to be a new SNR based both on our FUV and optical data, and X-ray and radio data presented by Becker et al. (2021). The presentation order follows that of our research work.

3.1. The Suspected Radio SNR G354.0-33.5

Using a 1420 MHz linear polarization survey of the southern hemisphere sky, Testori et al. (2008) identified a large $\sim\!10^\circ$ depolarized shell at $\alpha(\rm J2000)=20^{\rm h}25^{\rm m},\,\delta(\rm J2000)=-47^\circ,$ roughly corresponding to Galactic coordinates $l=353^\circ\,b=-34^\circ.$ This shell could also be seen in a 1.4 GHz polarization all-sky survey map (Reich & Reich 2009). Due to the object's spherical morphology and radio properties, Testori et al. (2008) suggested an SNR identification with a size suggesting a distance between 300 and 500 pc, a physical diameter of 17.4 pc $\times\,d_{100~\rm pc}$, and a z distance of 57.4 pc $\times\,d_{100~\rm pc}$. Testori et al. (2008) noted that the

object could be seen in 408 MHz data (Haslam et al. 1982) and weakly in the SHASSA H α images (Gaustad et al. 2001). This object also shows up in gradients of linearly polarized synchrotron radio emission (Iacobelli et al. 2014). More recently, Bracco et al. (2020) briefly commented on the presence of some GALEX FUV filaments coincident with this radio shell.

However, to our knowledge, there is no work showing this suspected SNR's FUV emissions or any associated optical emissions. Below we present large mosaics of GALEX FUV images along with an SHASSA ${\rm H}\alpha$ image and compare these to the low-resolution 1420 MHz radio images.

3.1.1. Far-UV and Ha Images

Figure 2 shows a wide-field mosaic of GALEX FUV images of G354–34 smoothed by a nine-point Gaussian. The image mosaic reveals a large, coherent set of sharp UV-emitting

filaments arranged in a fairly circular and complete shell-like structure, which is positionally coincident with the $1420\,\mathrm{MHz}$ radio shell. 13

Multiple and overlapping filaments are common along the shell's northern and western limbs. Because these filaments appear brightest in the GALEX FUV images compared to NUV images, we will concentrate mainly on the shell's far-UV emission structure.

Although many of the FUV filaments are unresolved at GALEX's 4."6 FWHM resolution, some filaments appear partially resolved in places, especially along its northernmost edge. It is not clear if this appearance is due to closely spaced multiple filaments or the resolution of a single emission filament.

The strong shock-like morphology of these filaments and their arrangement in a nearly continuous shell lends support to Testori et al.'s (2008) suggestion for it to be a previously unrecognized Galactic SNR, albeit with unusually large angular dimensions and distance from the Galactic plane.

Based on its FUV filaments, we estimate a somewhat larger angular dimensions than the 10° cited by Testori et al. (2008). Instead, we find dimensions of $\simeq 11^{\circ}$ east—west and $\simeq 14^{\circ}$ north—south, with a distinct indentation along its southwestern limb. Its southern extent is poorly constrained in our GALEX FUV mosaic but FUV filaments extend south to at least a decl. of $-53^{\circ}.5$. While largely coincident in location with the 1420 MHZ radio emission map of Testori et al. (2008), the $\sim 11^{\circ}$ east—west diameter seen in the FUV images is centered around $20^{\rm h}16^{\rm m}$, $-45^{\circ}.50'$ ($l=354^{\circ}.0$, $b=-33^{\circ}.5$). Hence, we will use the shorten name G354–33 based on the FUV images (see Table 1), which is slightly different from the G353–34 name cited by Testori et al. (2008).

Due to its large size, many of the filamentary details visible in the full-resolution FUV mosaic are lost in Figure 2. Consequently, we show in Figure 3 blowups of four regions, along G354–33's northern, western, southeastern, and southwestern rims to give a better sense of the object's fine-scale UV emission structure and morphology. Note that some individual filaments are 2° – 3° in length, equivalent to the diameters of some of the largest confirmed Galactic SNRs.

A continuum-subtracted SHASSA $H\alpha$ image mosaic of the G354–33 remnant is shown in Figure 4. This image reveals a thick diffuse shell of emission located within the boundaries of the FUV filaments. The $H\alpha$ emission structure is far more diffuse and broader than that seen in the GALEX FUV image with very few obvious thin filaments. We estimate an $H\alpha$ flux of around $(1-2)\times 10^{-17}\,\mathrm{erg}\,\mathrm{cm}^{-2}\,\mathrm{s}^{-1}\,\mathrm{arcsec}^{-2}$ for most of the diffuse emission and about three times this for the area of brighter emission along the nebula's northwestern limb.

While its $H\alpha$ emission's location matches that seen in the FUV image, some weak $H\alpha$ emission is seen to extend farther to the east and south than is readily visible in the GALEX FUV mosaic image. In general, however, the FUV filaments appear to mark the outer edges of the diffuse $H\alpha$ emission shell.

This is shown in Figure 5 where we compare FUV versus $H\alpha$ images for two northeastern sections along its limb. The upper images show the presence of weak $H\alpha$ emission coincident with the bright main section of the FUV filament, with diffuse $H\alpha$ emission extending toward the east bordered

by the long FUV filament. The lower panels show a section along the nebula's northeastern limb where again the UV filaments are seen to mark the extent of the diffuse ${\rm H}\alpha$ emission. The SHASSA image also gives a hint of filamentary structure that resembles that seen in the FUV image.

Higher-resolution optical images give a better sense of the remnant's true emission structure. Figure 6 presents a higher-resolution CHILESCOPE $H\alpha+[N\ II]$ image of a small portion of G354–33's northwestern limb where Figure 4 revealed a particularly bright emission patch. The upper panel of this figure shows this emission patch to be diffuse and situated mainly west of a \sim 45′ long, thin $H\alpha$ filament, which likely marks the western extent of the remnant in this region.

The three lower panels of Figure 6 compare the emission appearance of this $H\alpha$ filament in the GALEX FUV image and in an equally deep [O III] image. The similarity of the filament as seen in the FUV and $H\alpha$ images suggests G354–33's optical structure would consist of numerous thin, unresolved filaments like that seen in the FUV mosaic image shown in Figure 2.

Based on the filament's lack of [O III] emission, its thin morphology, and its brightness in the UV, it is likely to represent a nonradiative or a "Balmer-dominated" emission filament. Given the sharpness of the other G354–33 filaments in the FUV, they are also probably Balmer-dominated emission filaments marking the location of the object's shock front and outer boundary.

3.1.2. Radio and X-Rays

As already noted, Testori et al. (2008) used 1420 MHz Villa Elisa radio data (Testori et al. 2001) to identify the radio emission ring, G354–33, as a possible SNR. The upper panel of Figure 7 shows a $60^{\circ} \times 25^{\circ}$ wide section of the Villa Elisa 1420 MHz polarization southern sky survey data. The emission ring appears distinct in shape and separate from other emission features along the southern edge of the Galactic plane (i.e., the right-hand side of the image).

The images in the lower panels of Figure 7 show the GALEX FUV image mosaic (left panel) and the SHASSA ${\rm H}\alpha$ image (right panel) overlaid with the 1420 MHz Villa Elisa radio image contours. Overall, there is good agreement in both size and location for the FUV and ${\rm H}\alpha$ emission shells and radio ring seen in these images. This includes the greater extent toward the southern limb area. We note that the brightest portion of the radio emission lies on the object's western limb, the side facing the Galactic plane.

Examination of ROSAT online data showed no obvious associated X-ray emission with this nebula. This is not surprising given its location 33°.5 below the Galactic plane. Moreover, in view of the lack of any bright FUV emission nebulae along its limbs, this suggests that it lies in a region with few or no large-scale interstellar clouds that might generate significant X-ray flux.

3.2. SNR G249.7+24.7

Using GALEX FUV mosaics, we discovered a region containing several long, thin, shock-like morphology filaments aligned mostly N–S and arranged in a roughly elliptical shape $\sim 2^{\circ}.5 \times 4^{\circ}.0$ in size. These filaments appear centered at $\alpha(J2000) = 9^{h}30.5^{m}$ $\delta(J2000) = -16^{\circ}40'$. However, as discussed below, we believe the object to be larger and centered at

 $[\]overline{^{13}}$ Because of distortions due to the large size of this emission structure, the coordinates shown are only accurate to a few arcminutes.

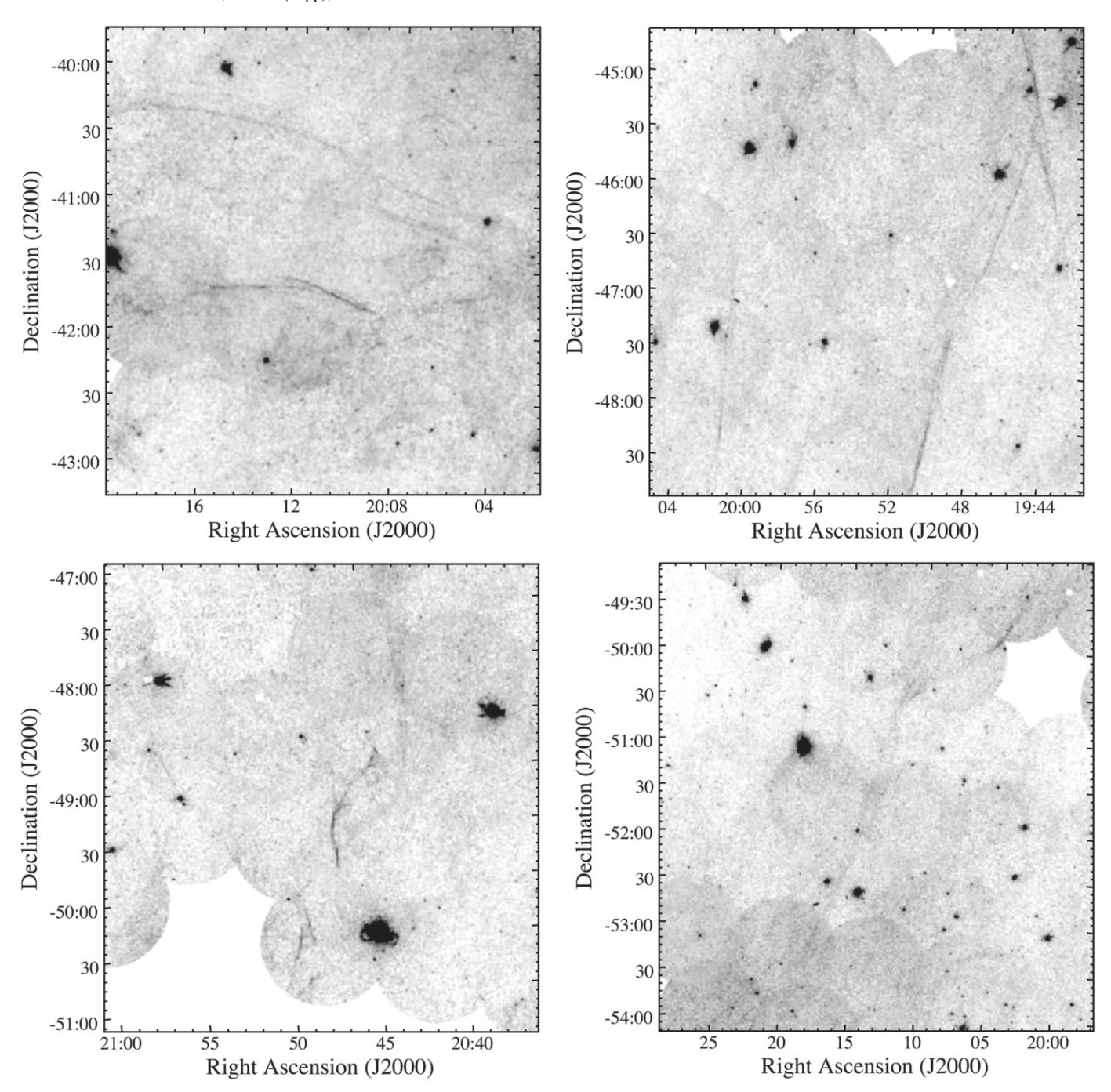


Figure 3. Blowups of the GALEX FUV mosaic of G354–33 along the remnant's northern (upper left), western (upper right), southeastern (lower left), and southwestern (lower right) limbs.

 $\alpha({\rm J2000})=9^{\rm h}33^{\rm m}~\delta({\rm J2000})=-17^{\rm o}00',$ which corresponds to Galactic coordinates $l=249^{\circ}.7$, $b=+24^{\circ}.7$. We call this object G249+24 for short. Below, we present images of this object's UV and H α emission structure along with optical spectra of four of its filamentary regions.

3.2.1. Far-UV Mosaic Image

Figure 8 presents a $5^{\circ}.2 \times 5^{\circ}.2$ mosaic of GALEX FUV images centered on G249+24's. The image shows several UV filaments along with a few smaller diffuse emission patches. Although GALEX imaging of this region is fairly incomplete,

enough imaging exists to indicate G249+24's minimum size and extent. 14

The nebula's brightest UV filaments are concentrated in its southern region where there is a bright, long gently curved filament along its southwestern edge. This feature itself consists of several separate, closely aligned filaments. Although a smaller but a similarly bright filament caught on the western edge of a more northern GALEX image might give the impression that this filament's full length and extent are

 $^{^{\}overline{14}}$ The bright feature at $9^{\rm h}30^{\rm m}$, $-17^{\circ}30'$ is HD 82093, an Ap(EuSrCr) star; V=7.08.

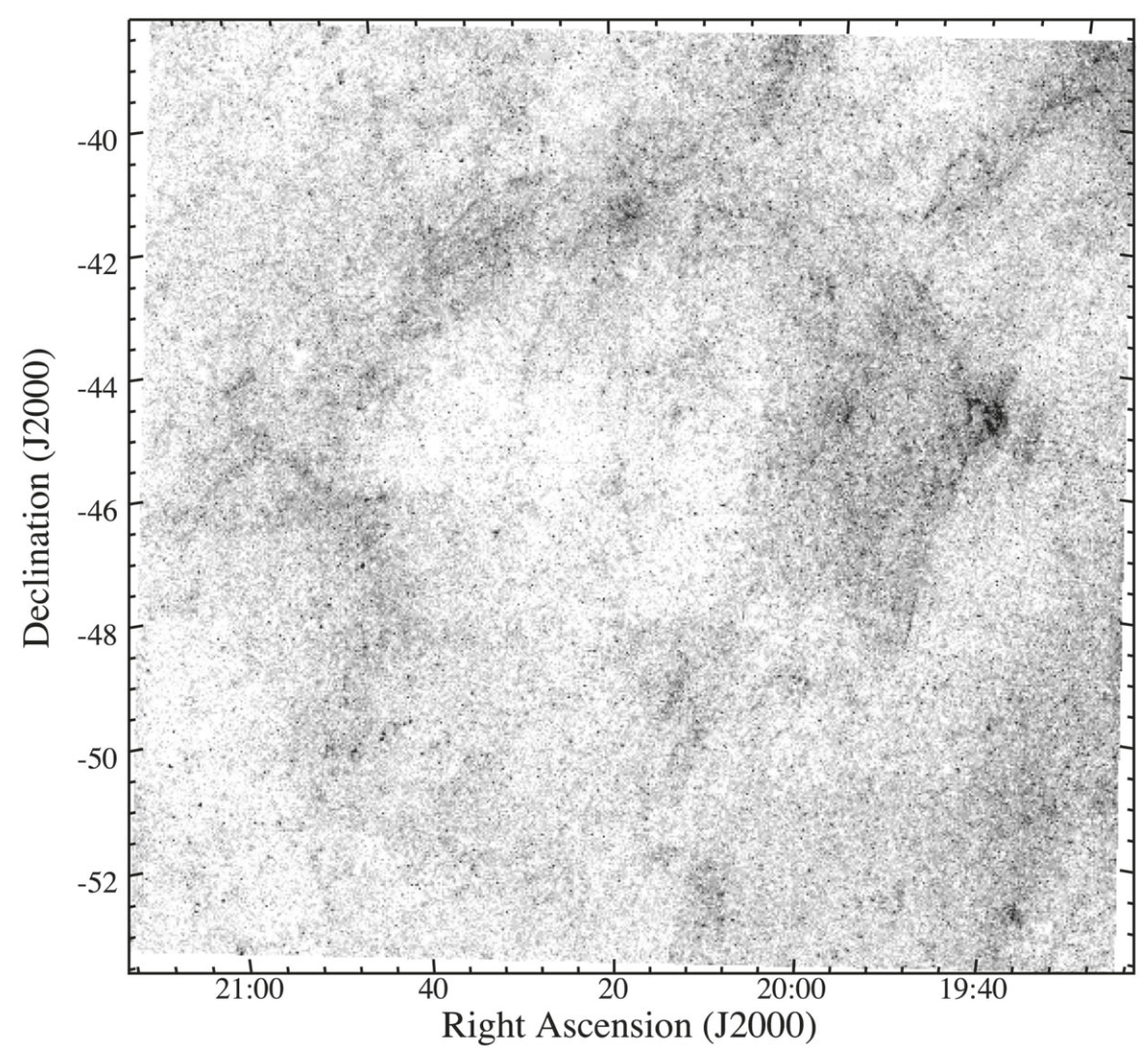


Figure 4. Continuum-subtracted SHASSA H α image of G354–33.

partially missing in this mosaic, this is not the case based on the $H\alpha$ images (see below).

3.2.2. Ha Emission

Whereas the object's FUV emission filaments are readily apparent in the GALEX image mosaic shown in Figure 8, its optical emissions are relatively faint. Although some of its brighter filaments are weakly visible on broad red passband Digital Sky Survey images, they are so faint and scattered over such a large area that it is not surprising that this nebula had not attracted prior attention.

The ${\rm H}\alpha$ images of the MDW All-Sky survey reveal more fully G249+24's optical emissions. In Figure 9, we show a side-by-side comparison of G249+24's central emission structure in GALEX FUV and the MDW ${\rm H}\alpha$ images. In general, there is a good agreement between the nebula's UV and ${\rm H}\alpha$ emissions. The bright FUV and curved southwestern filament show up strongly in ${\rm H}\alpha$ as does a shorter filament a degree to its east. Correlated UV– ${\rm H}\alpha$ emission is also seen along the upper-left-hand portion of Figure 8, where diffuse and filament type of emission is seen in both. (Note: Faint diffuse emission seen along the lower portion of the ${\rm H}\alpha$ image extends several degrees to both the east and west of the region

and hence does not seem to be connected to G249+24's other optical features (see also Figure 10 below)).

However, little in the way of $H\alpha$ emission can be seen along the object's southeast limb, where in contrast one finds considerable FUV emission. A similar difference between FUV and $H\alpha$ fluxes is seen for the south-central area around 9^h28^m , $-18^\circ15'$. Consequently, it is clear that this nebula's overall structure is more readily visible in the FUV than in even fairly deep $H\alpha$ images.

Higher-resolution MDM H α images of selected regions of the nebula were also obtained and presented in Figure 11. Although these images were taken mainly in preparation for follow-up spectral observations, they showed a surprising amount of filamentary detail in G249+24's optical emission than initially indicated in Figure 9. Numerous long and delicate filaments are visible in several of these images, indicating a rich and beautiful optical shock emission structure largely hidden due to its relative faintness.

3.2.3. Low-dispersion Optical Spectra

Low-dispersion, exploratory slit spectra were taken at four positions (P1 through P4) in G249+24 as shown in Figures 10 and 11 in order to investigate the emission nature of

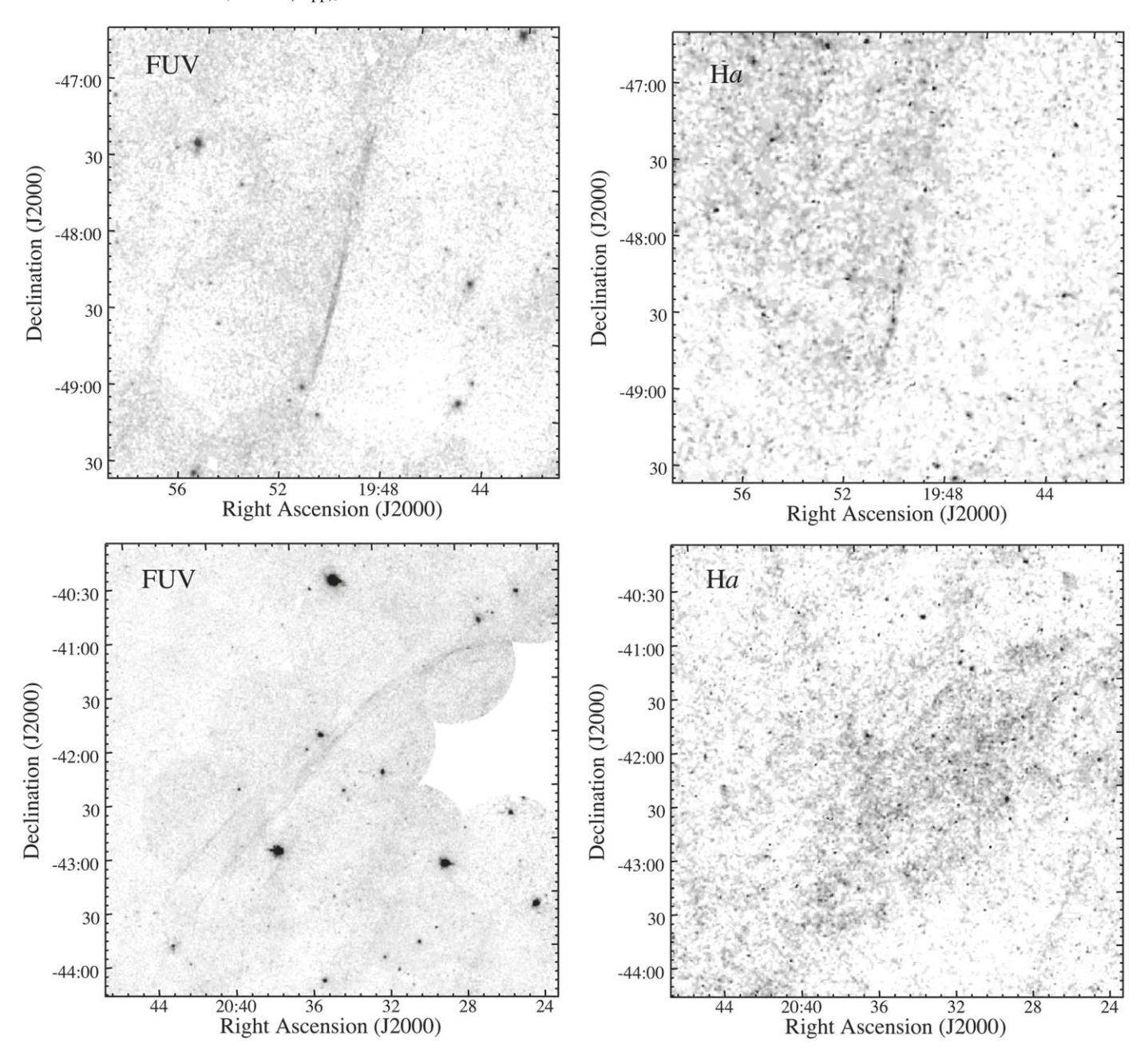


Figure 5. Matched GALEX FUV and continuum-subtracted SHASSA H α images for a bright filament along G354–33's western limb (upper panels) and northeastern limb (lower panels).

G249+24's optical filaments. Because only the spectra taken at P1 exhibited any [O III] emission, the four spectral plots shown in Figure 12 cover only the wavelength region 6200–6900 Å.

The resulting spectra reveal clear evidence for its filaments being shock-heated ISM like that commonly seen in SNRs. For example, spectra obtained at P2, P3, and P4 exhibited [S II]/ $H\alpha$ ratios of 1.26 ± 0.20 , 0.45 ± 0.04 , and 0.91 ± 0.15 , respectively, thus well above the standard criteria ratio of 0.40 indicative of shock emission. Added support for shocks is the detection of [O I] λ 6300 emission in the spectra of both P3 and P4. The presence of [O I] is a secondary indicator for shock emission commonly observed in evolved SNRs (Fesen et al. 1985; Kopsacheili et al. 2020).

The [S II] $\lambda 6716/\lambda 6731$ line ratio can be used to estimate the electron density in the S⁺ recombination zone and is nearly

independent of electron temperature (Osterbrock & Ferland 2006). The $\lambda 6716/\lambda 6731$ ratio was found to be near the low-density limit of 1.43, indicating $n_e < 100~{\rm cm}^{-3}$, 1.48 \pm 0.04 for P2, and 1.42 \pm 0.03 for P4. A bit surprisingly, this ratio for P3 was observed to be \simeq 1.15 indicating an n_e density much higher than the other locations of around 500 cm⁻¹. Interestingly, the spectrum seen at P3 also showed much weaker [N II] $\lambda 6583$ line emission compared to that seen at P2 and P4.

The spectrum taken at P1 deserves special attention due to significant line emission variations with respect to distance along the E–W-aligned slit. This is shown in Figure 13, where line emission can be seen to start at the location of the mainly N–S-aligned filament extending many arcseconds to the east (left). The emission-line ratio of ${\rm H}\alpha/[{\rm O\,III}]$ can be seen to vary considerably downstream from the shock front.

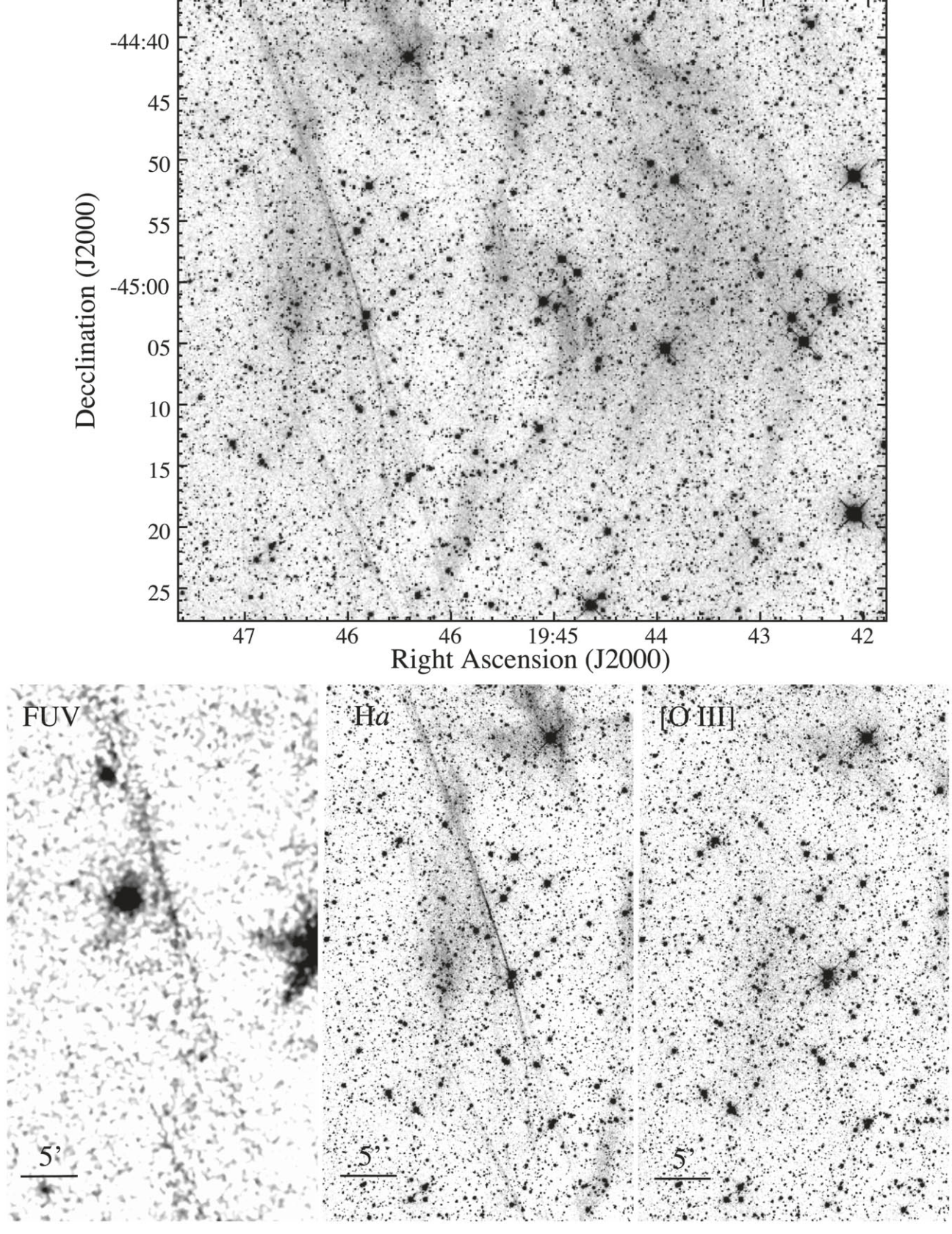


Figure 6. Top: CHILESCOPE $H\alpha+[N\ II]$ image of G354–33's northwest limb revealing emission structure details lost in the low-resolution SHASSA image shown in Figure 4. Bottom: matched GALEX FUV and CHILESCOPE $H\alpha$ and $[O\ III]$ images for the thin filaments seen in this NW region. The thin filament is clearly seen in the FUV and $H\alpha$ images but not in $[O\ III]$.

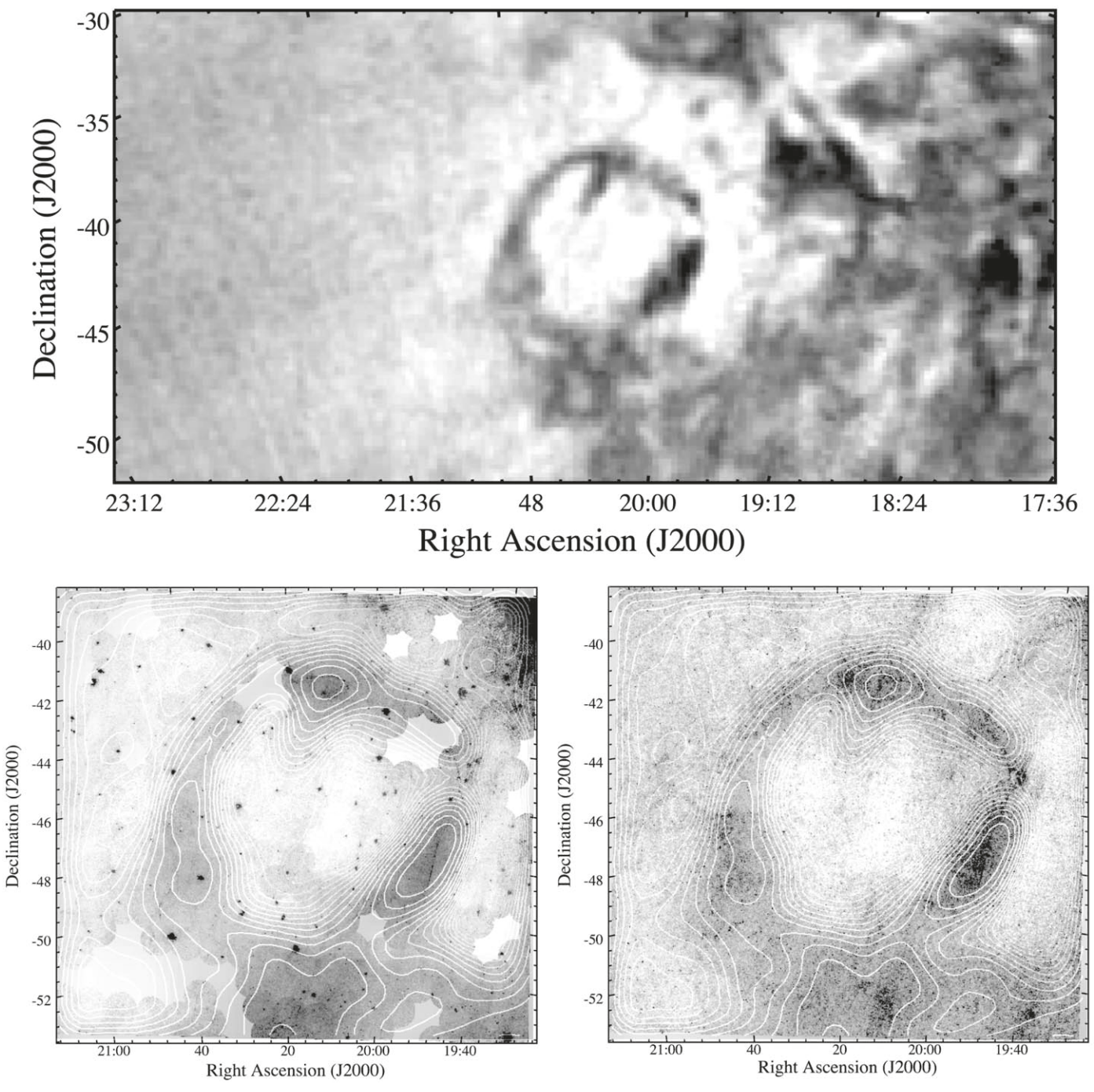


Figure 7. Upper panel: 1420 MHz Villa Elisa Stokes Q polarization intensity image covering a $60^{\circ} \times 25^{\circ}$ region centered on G354–33. Lower panels: contour overlays of the Villa Elisa radio emission with the GALEX FUV (left) and SHASSA H α (right) images of the G354–33 region showing excellent size and positional agreement of the 1420 MHz radio emission ring with the filamentary shell of the far-UV and H α emission filaments.

Figure 13 also shows the 2D image of the background-subtracted P1 spectrum for the areas around H α , [O III] $\lambda\lambda4959,5007$ and H β . This figure shows a clear separation of the filament's Balmer-dominated emission followed by strong [O III] emission resulting in large [O III] $\lambda5007/\text{H}\alpha$ ratios. The arrows indicate the section where the P1 spectrum shown in Figure 11 was taken.

Behind the leading edge of the shock front marked by the start of line emissions, $H\alpha$ emission becomes strong with little or no emission in other lines. The intensity of $H\alpha$ then briefly drops in strength within a distance of a few arcseconds, then

increases for a short distance followed by a long, gradual decline. The [O III] emission is barely detectable at the shock front where the H α starts but substantially increases some 10''-20'' behind the shock front, where it dominates the downstream spectrum. This is consistent with the picture of an extended postshock cooling zone. The presence of such strong [O III] emission behind the shock front suggests shock velocities at least $100~{\rm km\,s^{-1}}$ are present in certain filaments. In contrast, spectra at P2, P3, and P4 showed no appreciable [O III] emission, indicating much lower-velocity shocks, less than about $70~{\rm km\,s^{-1}}$.

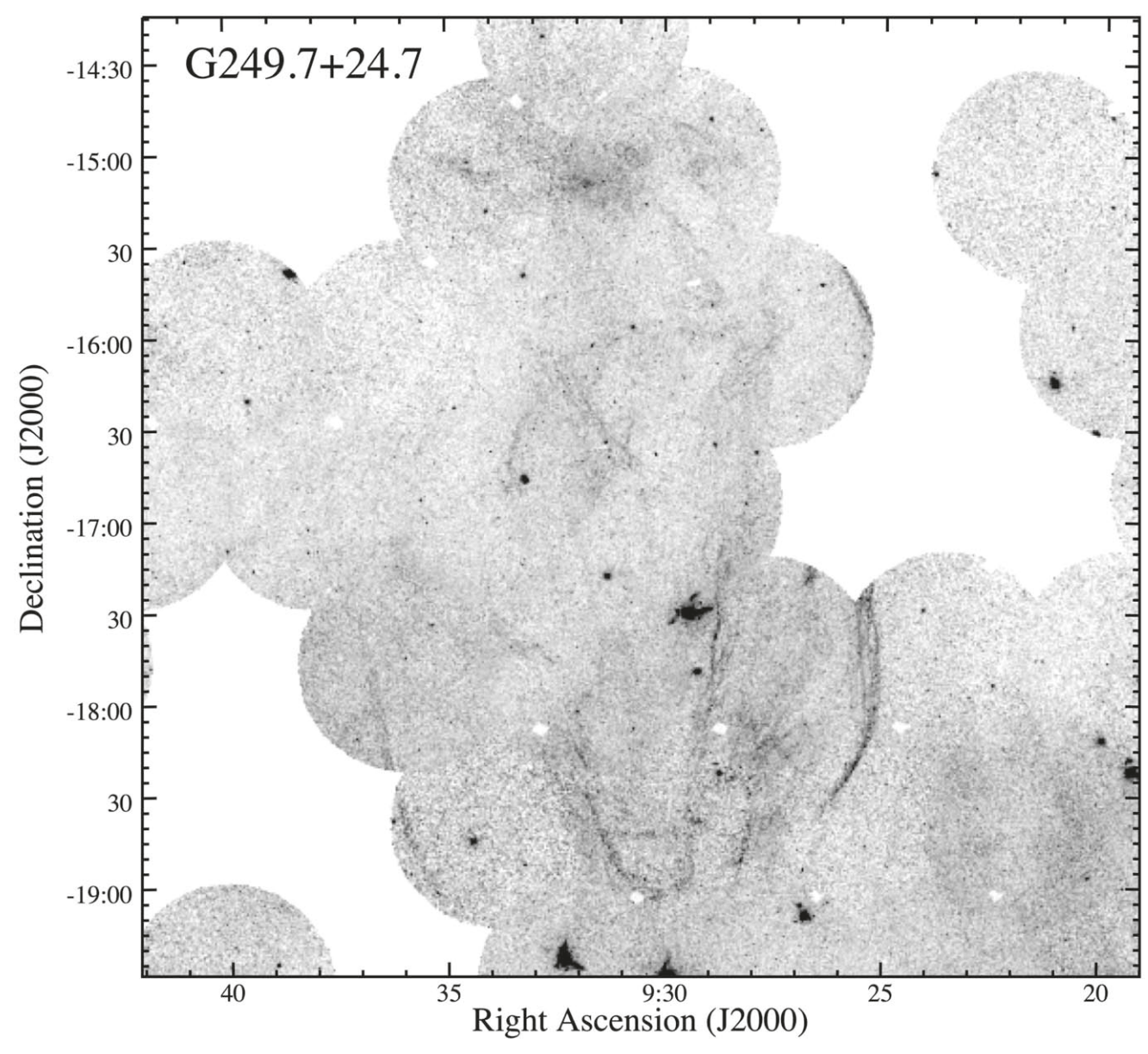


Figure 8. FUV intensity map of G249+24 showing an elliptical-shaped shell of UV emission filaments.

Similar 2D emission structures have been observed in the high-latitude Galactic halo SNRs G70.0-21.5 (Raymond et al. 2020) and G107.0+9.0 (Fesen et al. 2020). They can be interpreted as emission from a $\sim 100 \, \mathrm{km \, s^{-1}}$ shock in partially neutral gas. Neutral hydrogen atoms swept up by the shock are quickly ionized, but before that happens, some of them are excited to produce $H\alpha$. This emission region is very thin. It is followed by a thicker ionization zone where O II is ionized to O III. As the gas cools, the [O III] fades and H α brightens. In the case of G107.0+9.0, the 10'' gap between $H\alpha$ and [O III] and the $\sim 10''$ wide diffuse patch of [O III] emission are well matched by models of 100 km s⁻¹ shocks in a gas of density 0.1 cm⁻³ at a distance of 1 kpc (Fesen et al. 2020). The wider patch of [O III] diffuse emission at Position 1 of G249+24 suggests a longer cooling length, as would occur in a slightly faster shock, perhaps $\sim 120 \, \mathrm{km \, s^{-1}}$. These structures are spatially resolved, thanks to the low density of the Galactic halo and the relatively small distances to these SNRs.

The flux level of $H\beta$ was either undetected or too faint at P2, P3, and P4 to accurately measure an $H\beta/H\alpha$ ratio, which could be used to estimate extinction. Only the spectrum P1 showed a weak but measurable level of $H\beta$ flux. There the measured $H\alpha/H\beta$ ratio of 2.85 ± 0.20 suggests a very low amount of extinction. Adopting a theoretical $H\alpha/H\beta$ ratio of 2.87 for 10^4 K, we estimate a foreground E(B-V) < 0.07. However, in view of the weakness of the $H\beta$ detection, this estimate comes with a large uncertainty. Nonetheless, such a low interstellar extinction is not unexpected due to the remnant's high Galactic latitude of $24^\circ.4$.

If this low-extinction estimate is correct, then the lack of [O III] emission at P2, P3, and P4 suggests a fairly low shock velocity, around $70~\rm km~s^{-1}$ or less, in contrast to that indicated at P1. Consequently, it appears that a variety of shock speeds, from $<\!70~\rm to \geqslant\!120~km~s^{-1}$, appear to be present throughout the nebula's structure. This conclusion is supported by the Na I absorptions described below.

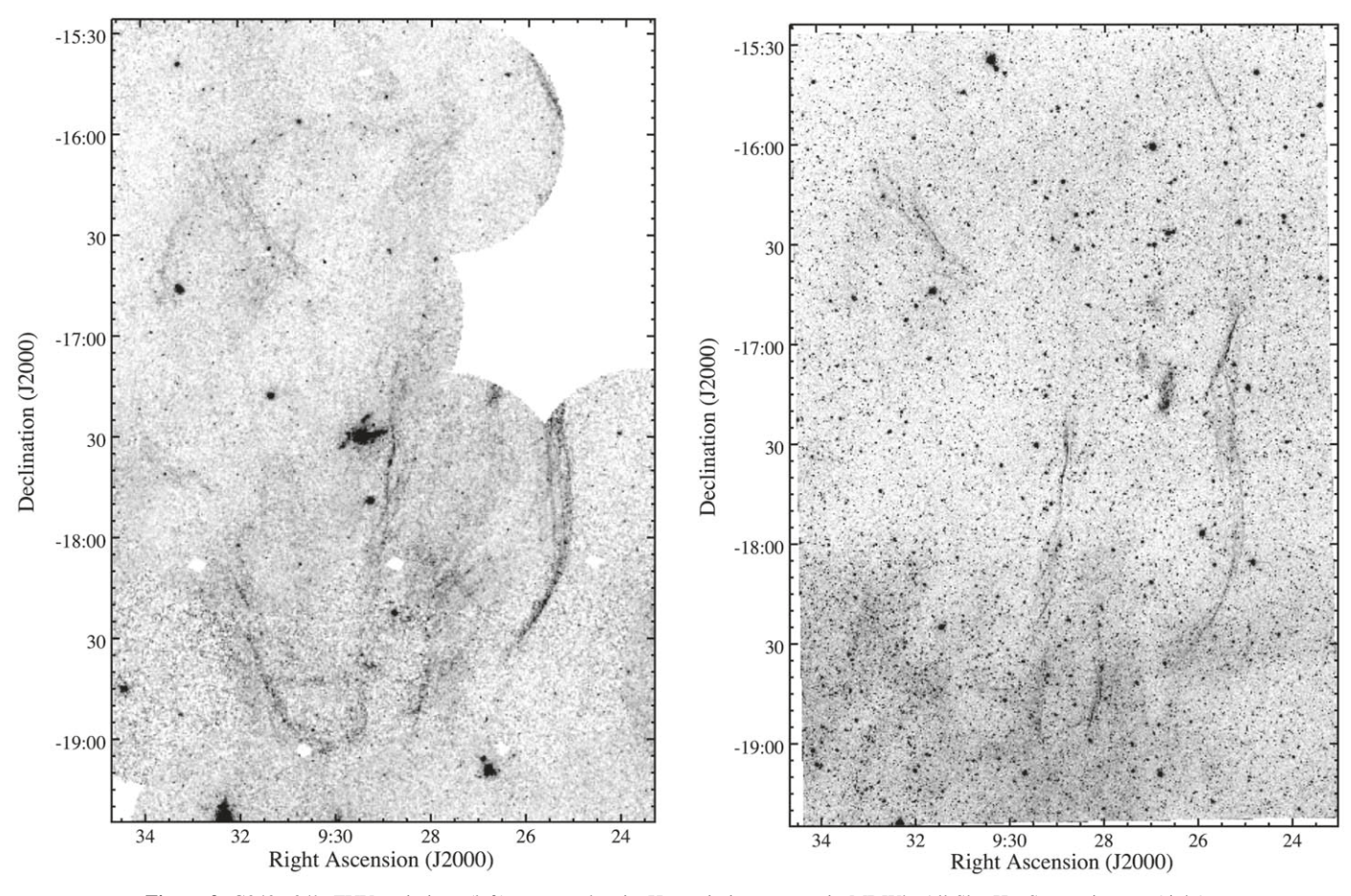


Figure 9. G249+24's FUV emissions (left) compared to its H α emission as seen in MDW's All-Sky H α Survey images (right).

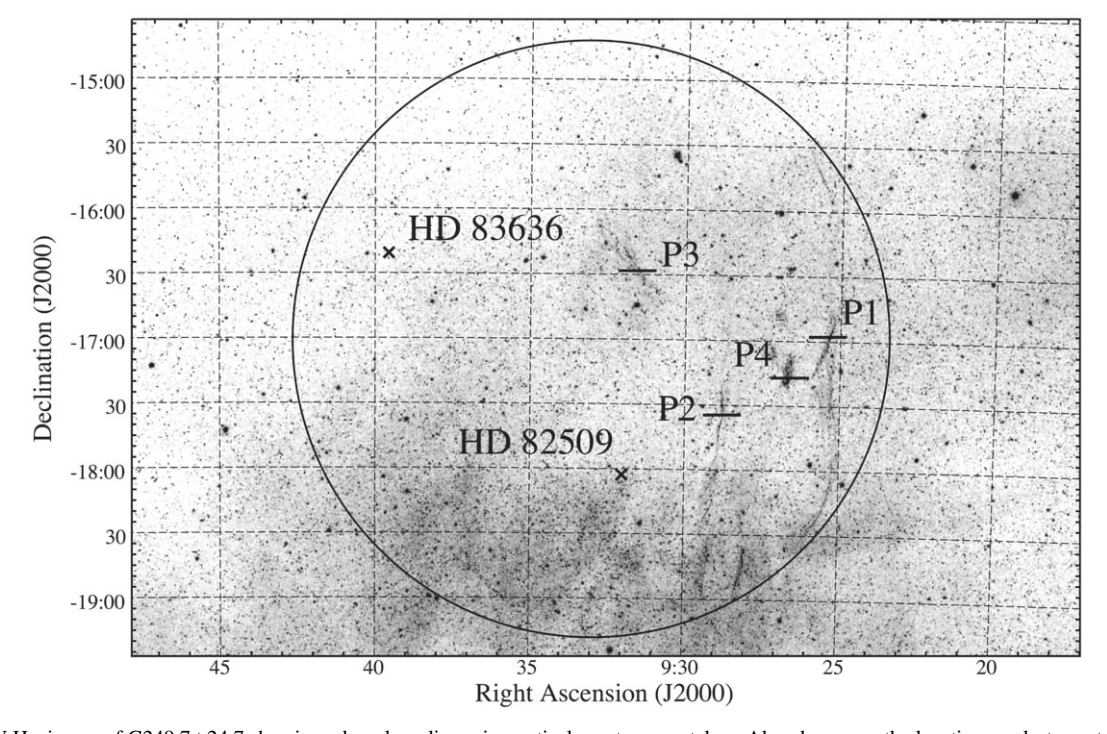


Figure 10. MDW $H\alpha$ image of G249.7+24.7 showing where low-dispersion optical spectra were taken. Also shown are the locations early-type stars HD 82509 and HD 83636, which were found to exhibit high-velocity Na I absorption features. The black circle (dia. = 4.5) marks the approximate size of the remnant.

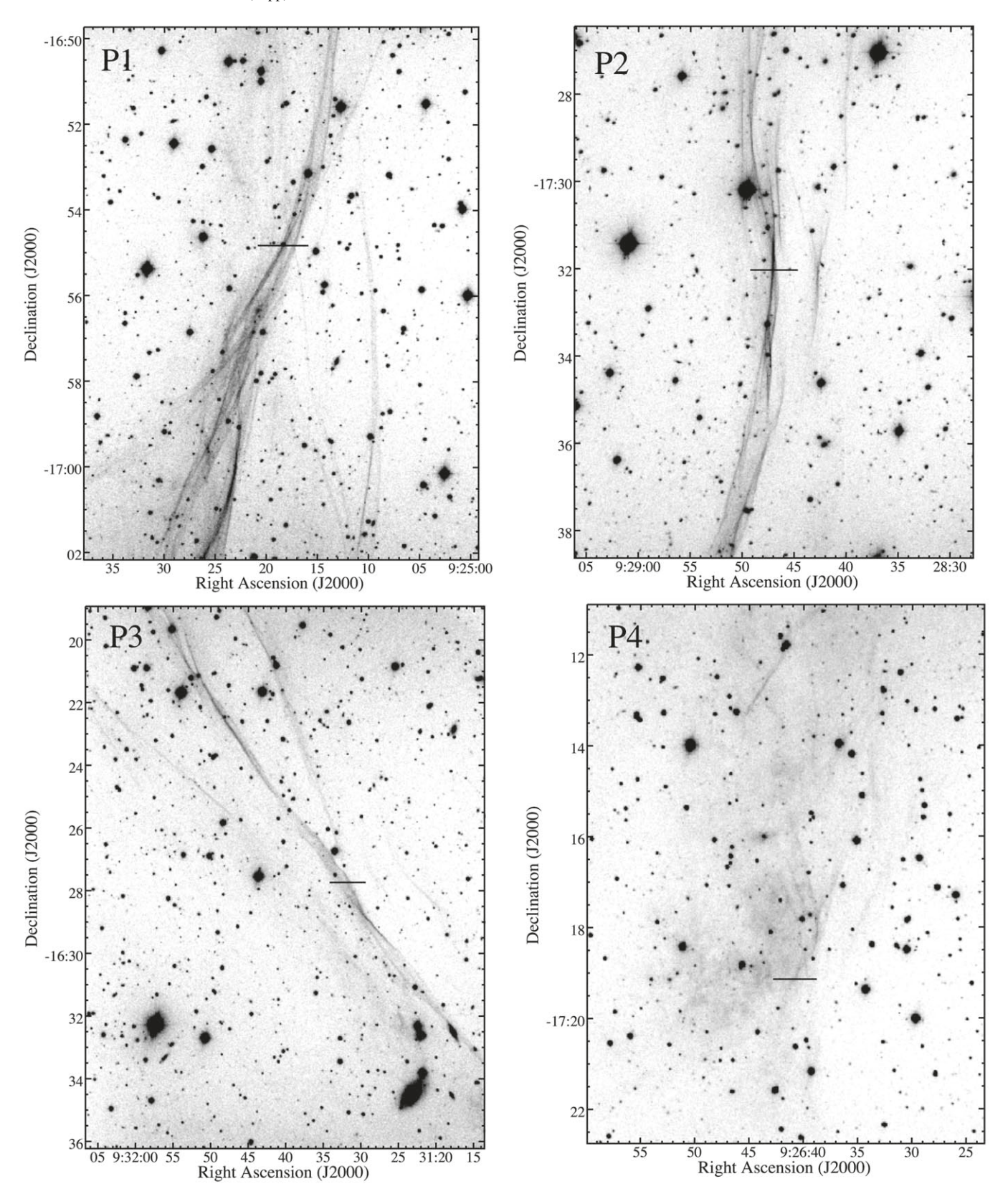


Figure 11. MDM $H\alpha+[N\ II]$ images of filaments showing locations of slit Positions 1 and 2. Slit lengths as shown are 1' in length. Note the numerous long, fine filaments in these regions, which are common characteristics of SNR shocks.

3.2.4. High-velocity Na I Absorption Lines

Moderate-dispersion optical spectra ($R \simeq 7200$) of several stars with projected positions within the estimated radio boundary of

G249+24 (see Becker et al. 2021 and Section 3.2.5 below) were obtained in a search for high-velocity Na I interstellar absorption components, which could yield both a direct measurement of its

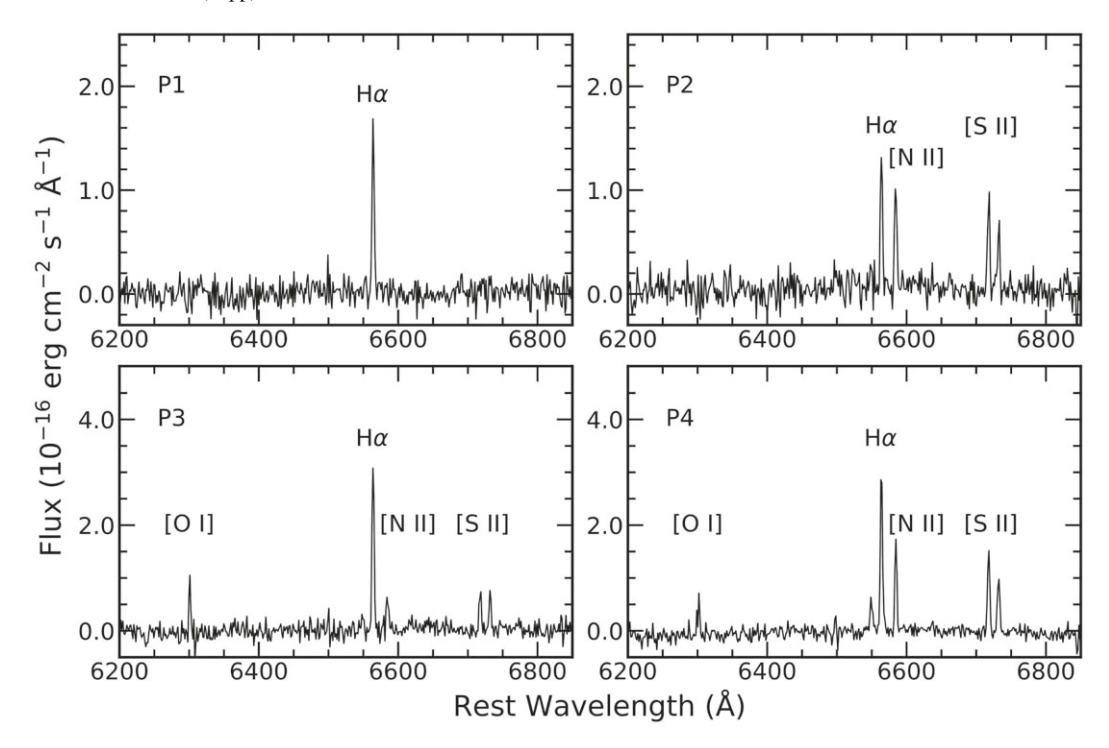


Figure 12. Optical spectra of filamentary emission at positions in G249+24.

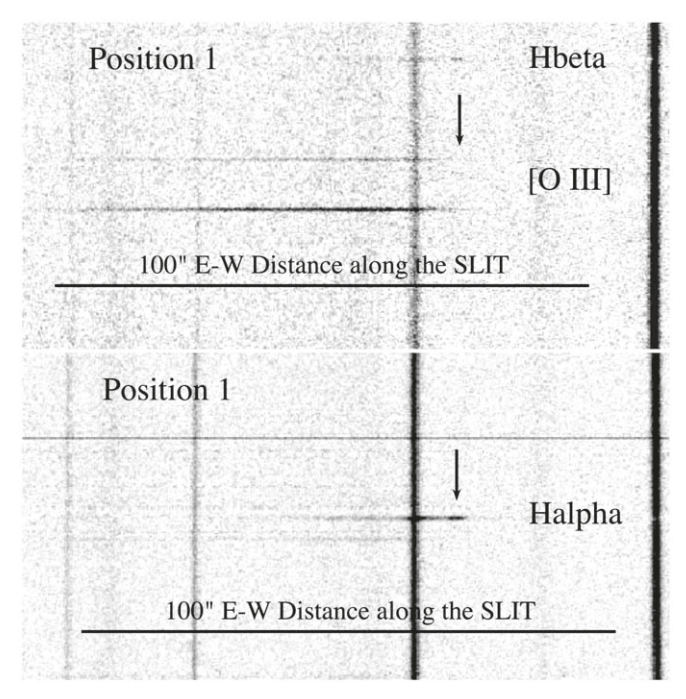


Figure 13. Sections of the long-slit spectra for Position 1. Both [O III] λ 4959 and λ 5007 lines are visible in the upper panel.

expansion velocity plus maximum remnant distance information. Of the stars examined, two showed evidence for the presence of high-velocity (>40 km s⁻¹) Na I absorption features.

The two stars were HD 82509 (B=10.29, V=10.4; A2 IV) with an estimated Gaia Early Release DR3 (EDR3) distance estimate of 825 ± 25 pc, and HD 83636 (B=9.74, V=9.57: A2 IV/V) with an EDR3 distance estimate of 386 ± 4 pc. Figure 10 shows the locations of these stars relative to the object's FUV and optical emissions.

Reduced and normalized spectra of both stars for the wavelength region around the Na_I D lines at λ 5889.95 and λ5895.92 indicating the presence of high-velocity Na I absorptions are shown in Figure 14. Using IRAF deblending software and allowing initially chosen absorption component wavelengths to vary but keeping the Gaussian line profiles and FWHMs all the same, we found red and blue absorption features in the observed Na I profiles in both stars with LSR velocities around +55 to -73 km s⁻¹. In addition, to achieve a good fit to the Na absorption in the spectrum of HD 83636, an additional blueshifted component with a radial velocity of around $-123 \,\mathrm{km \, s}^{-1}$ was needed (see Table 3). We note that the lower-velocity components are consistent with the observed spectra seen for slit positions P2, P3, and P4 where no [O III] was seen, indicating shock velocities below $\simeq 70 \,\mathrm{km \, s^{-1}}$, while the presence of the higher velocity 123 km s⁻¹ component is consistent with the strong [O III] seen at slit position P1.

The detection of these high-velocity Na I absorptions in these two stars can be used to estimate a maximum distance to G249+24. HD 82509's Gaia EDR3 parallax derived distance sets a distance limit of less than 825 pc, while HD 83636 sets a maximum distance of less than 390 pc. Assuming an angular diameter of 4°.5 (see below), this shorter maximum 390 pc distance implies a maximum physical size for G249+24 of \sim 30 pc, similar to that estimated for the Cygnus Loop SNR (Fesen et al. 2018).

3.2.5. Associated Radio and X-Ray Emissions

Examination of several online radio maps including the NRAO VLA Sky Survey (NVSS; Condon et al. 1998) did not show obvious radio emission in the G249+24 region. However, the 1420 MHz Bonn survey (Reich 1982) did show some emission along G249+24's FUV and optical filaments near $\alpha(J2000) = 9^h$ 27.5^m, $\delta(J2000) = -16^{\circ}10'$.

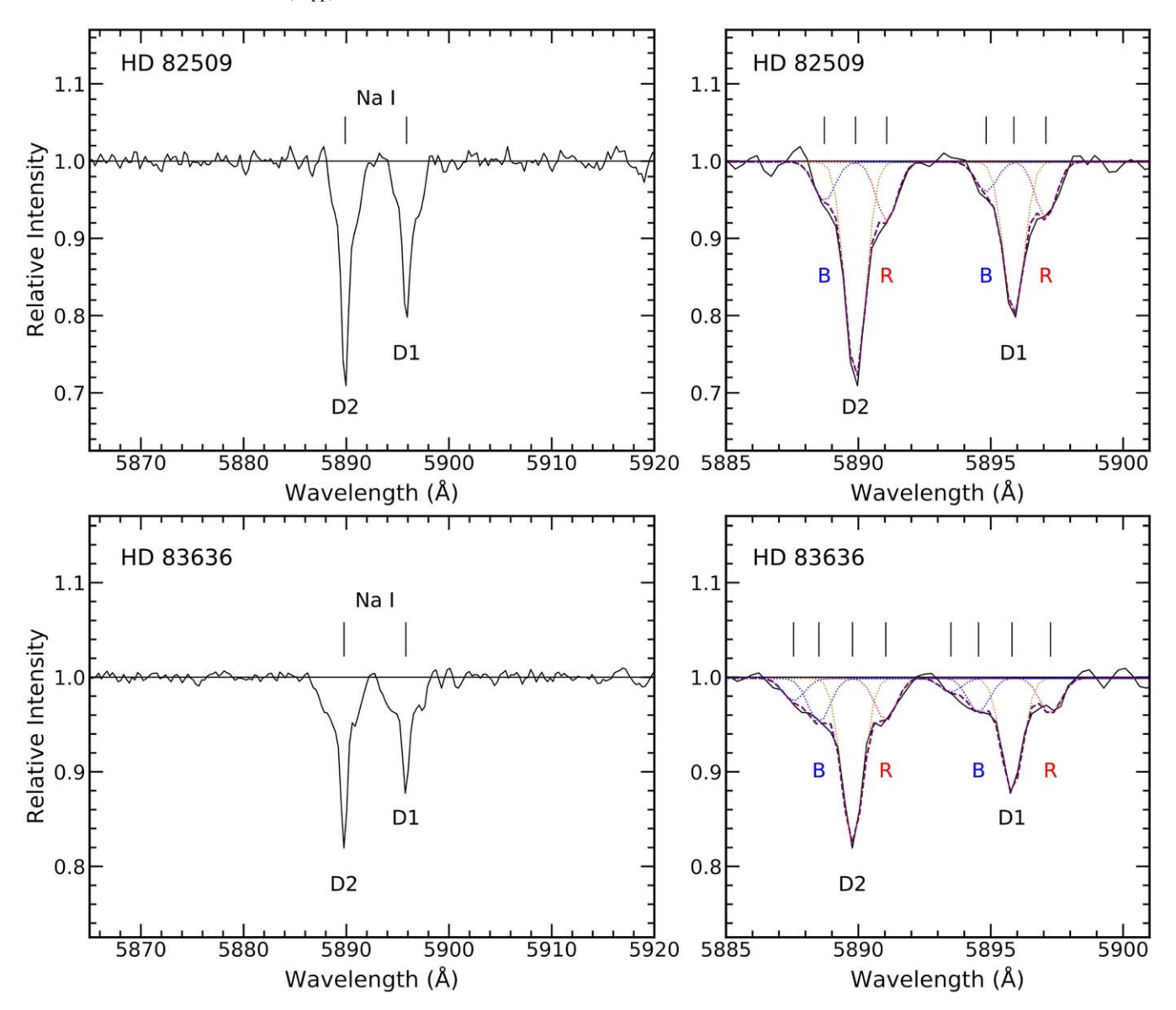


Figure 14. Moderate-dispersion CCDS spectra of HD 82509 (top) and HD 83636 (bottom) showing the deblending of the Na I lines into high-velocity blue and redshifted absorption components associated with G249+24. See Table 3.

Table 3
Measured Interstellar Na I Velocity Components and Equivalent Widths

Star ID	Distance (pc)	Na I Line	$\frac{V_0}{(\mathrm{km\ s}^{-1})}$	EW ₀ (Å)	V_{R1} (km s ⁻¹)	EW _{R1} (Å)	$V_{\rm B1}$ (km s ⁻¹)	EW _{B1} (Å)	$V_{\rm B2}$ (km s ⁻¹)	EW _{B2} (Å)
HD 82509	825 ± 25	λ 5889.95	-3	0.28	+57	0.08	-63	0.05	•••	
		λ 5895.92	-2	0.20	+59	0.08	-56	0.04		
HD 83636	386 ± 4	λ 5889.95	-9	0.17	+55	0.05	-73	0.05	-122	0.02
		λ 5895.92	-6	0.12	+70	0.04	-70	0.04	-123	0.01

The 408 MHz all-sky survey (Haslam et al. 1981, 1982) also showed enhanced emission in a roughly spherical shape approximately 4°.5 in diameter centered at 9^h32.7^m, -16°45′, a position that is nearly the same as that indicated by FUV and optical images (see Figure 15). A seemingly unrelated broad, vertical emission feature borders the emission shell on its eastern side and complicates the assessment of this emission. Assuming this emission shell is associated with the nebula, it would suggest a

far more spherical SNR than indicated by either the GALEX FUV or MDW ${\rm H}\alpha$ images. Taking the object's largest N–S angular dimensions based on its FUV filaments (see Figures 8 and 9) and requiring that both stars, HD 82509 and HD 83636, must lie inside the remnant's shell, we estimate G249+24 is $\simeq\!4^\circ\!.5$ in diameter assuming a circular morphology. This size estimate is in excellent agreement with that found by Becker et al. (2021) using eRosite X-ray images and archival Parks All-Sky Survey radio data.

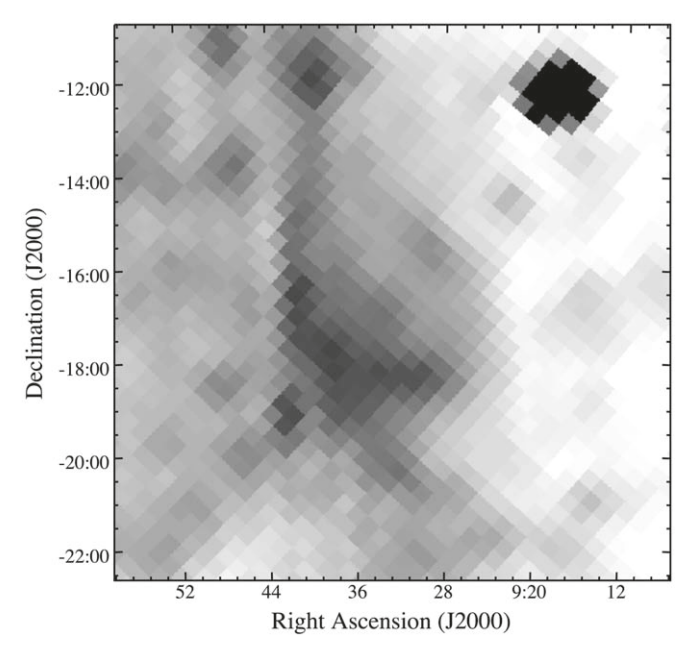


Figure 15. A 408 MHz intensity image of the G249+24 region from the Haslam et al. (1982) All-Sky survey.

Becker et al. (2021) report the detection of diffuse X-ray emission filling almost the entire remnant with a gas temperature of order kT=0.1~keV, along with radio data indicating a spectral index of -0.69 fully consist with its SNR nature.

3.3. The Exceptionally Large Suspected Antlia SNR

McCullough et al. (2002) reported a discovery of a very large ${\sim}24^{\circ}$ diameter $H\alpha$ emission shell with interior ROSAT 0.25 keV X-ray emission located in the southern hemisphere and at a high Galactic latitude of $+19^{\circ}$. They proposed it to be a previously unrecognized SNR and named it Antlia for the constellation it is found in. McCullough et al. (2002) suggested it was an extremely old remnant with an estimated age of ${\sim}1$ Myr and located relatively nearby with an uncertain distance of between 60 and 340 pc.

The Antlia remnant does appear in the catalog of high-energy SNRs (Ferrand & Safi-Harb 2012) but not in the Green (2019) catalog of confirmed Galactic SNRs, which cited the need for further observations to confirm its nature and parameters. Except for a 2007 far-UV study finding weak coincident C III λ 977 and C IV $\lambda\lambda$ 1548,1551 line emissions from the object's interior (Shinn et al. 2007) and a brief AAS abstract by Orchard et al. (2015) who reported Wisconsin H α Mapper data indicating [S II] emission from the Antlia Nebula consistent with an SNR interpretation, there has been no detailed follow-up investigation of this exceptionally large suspected SNR. This situation plus its location at an unusually high Galactic latitude led us to include it in our high Galactic latitude GALEX FUV investigation of SNRs.

3.3.1. GALEX FUV and MDW H\alpha Images

In the top panel of Figure 16, we present a mosaic of SHASSA $H\alpha$ images of the Antlia remnant at a higher resolution than the

VTSS H α image (Finkbeiner 2003), which led McCullough et al. (2002) to discover it. It shows a \sim 20° × 26° H α emission shell with a well-determined boundary roughly centered at α (J2000) = $10^{\rm h}38^{\rm m}$, δ (J2000) = $-37^{\circ}18'$ corresponding to Galactic coordinates $l=275^{\circ}.5$ $b=+18^{\circ}.4$. (Note: These Galactic coordinates differ slightly from those given by McCullough et al. 2002.)

A mosaic of FUV GALEX images covering just the remnant's northern limb is shown in the lower panel of Figure 13. This image reveals a long and nearly continuous set of thin, bright FUV emission filaments and filament clusters extending approximately 20° along the remnant's northeastern limb. The line of FUV filaments starts at R.A. = $10^{h}10^{m}$ and decl. = -24° and extends southward to the bottom left of the figure at R.A. = $11^{h}40^{m}$ and decl. = -32° .

Because the morphology of Antlia's FUV filaments is similar to that seen in the proposed SNRs G354–33 and G249+24, we examined MDW $H\alpha$ images of the FUV filaments and adjacent regions above the -32° decl. limit of the MDW survey. Overall, we found excellent positional agreement between FUV and $H\alpha$ filaments.

To illustrate this agreement, Figure 17 shows a comparison of GALEX FUV and MDW survey ${\rm H}\alpha$ images for three sections along the Antlia's northeastern boundary. While we find there is a close correlation of the outer FUV filaments with many ${\rm H}\alpha$ filaments, there are also considerable differences in terms of the nebula's internal emissions. That is, far more ${\rm H}\alpha$ emission is seen "behind," i.e., to the west, of the sharp, outlying filaments than seen in the FUV images. This is most striking in the lower panel images of Figure 16 for the remnant's southeastern limb region. While the SHASSA image shows considerable internal diffuse and filamentary emission, the brightest ${\rm H}\alpha$ emissions are found along Antlia's northwestern, western and southeast limbs.

3.3.2. Optical Spectra

If McCullough et al. (2002) are correct in their assessment that the Antlia ${\rm H}\alpha$ nebula is an SNR, as seemingly supported by the GALEX FUV and ${\rm H}\alpha$ images described above, the remnant would then be both many times larger than any confirmed SNR and be located at an unusually high Galactic latitude. On the other hand, considering its size and location immediately adjacent to the enormous Gum Nebula with its extended emission, outer "filamentary wisps," and numerous H I wind-blown bubbles (Brandt et al. 1976; Chanot & Sivan 1983; Purcell et al. 2015), there was uncertainty about its true origin.

Optical spectra are a powerful tool for confirming the presence of shock emission and hence can be used to investigate the SNR origin of optical nebulosities. Consequently, we obtained long-slit, low-dispersion spectra of seven filaments and emission clumps distributed across the whole of the Antlia nebula to explore the nature of its optical emissions.

Figure 18 shows the location of the seven filaments observed in the Antlia remnant, along with the resulting spectra. Table 2 lists the relative emission-line strengths uncorrected for extinction. Listed relative line strengths are believed accurate to 10%. Based on the observed $H\alpha/H\beta$ ratios of 3.0–4.30, we find a variable degree of extinction across the Antlia nebula, with E(B-V) values ranging from 0.0 to 0.35 assuming an

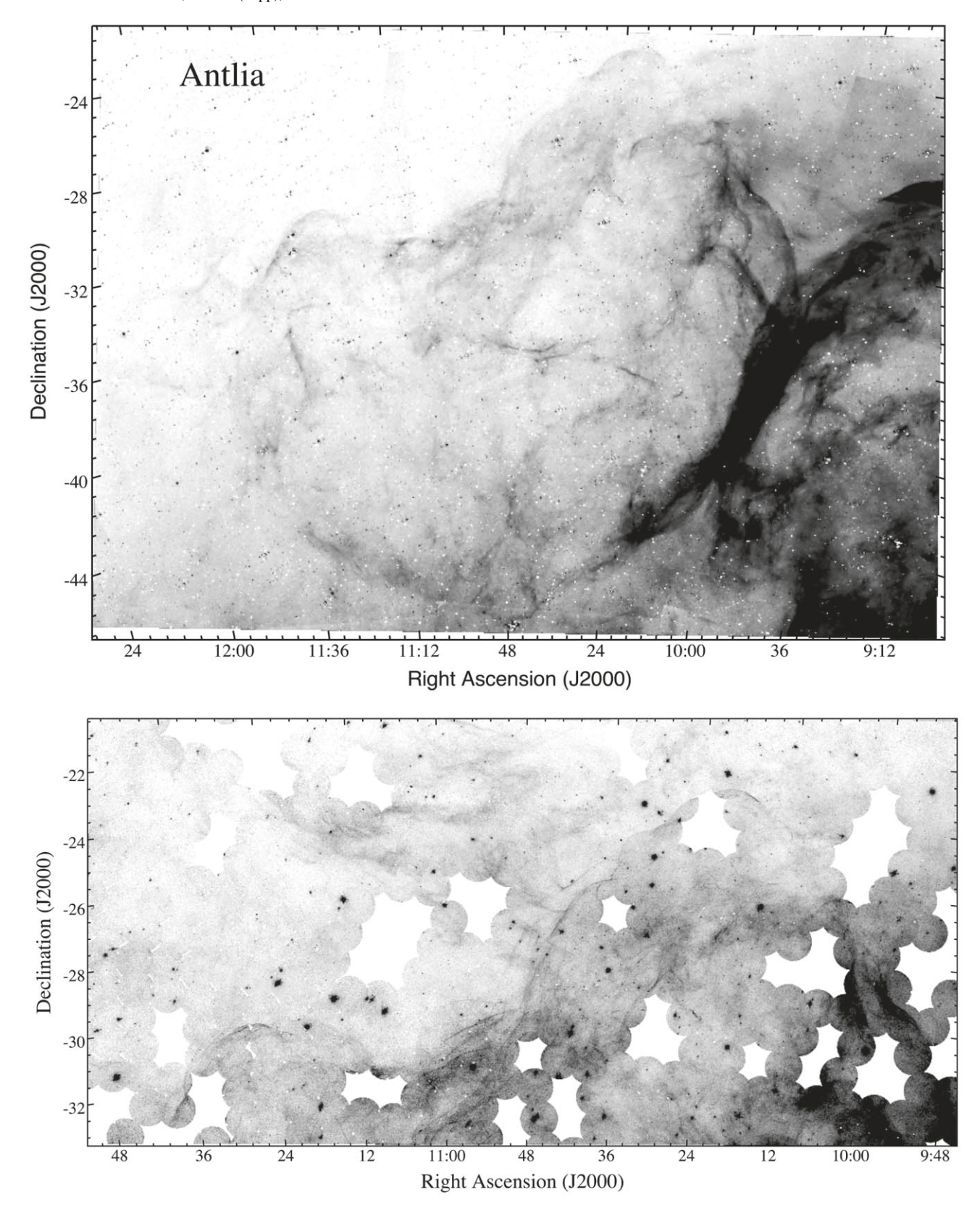


Figure 16. Top: continuum-subtracted SHASSA $H\alpha$ image mosaic of the Antlia remnant. Bottom: GALEX FUV mosaic showing a nearly unbroken line of UV emission filaments along Antlia's northern and eastern boundaries.

intrinsic ratio of 3.0 and an R value of 3.1. Here we have chosen an ${\rm H}\alpha/{\rm H}\beta$ value greater than the theoretical value of 2.87 for 10^4 K due to the likelihood of significant collisional

excitation of the n=3 level at postshock temperatures seen in SNRs. Such a range of extinction values is not unexpected in view of the nebula's large dimensions.

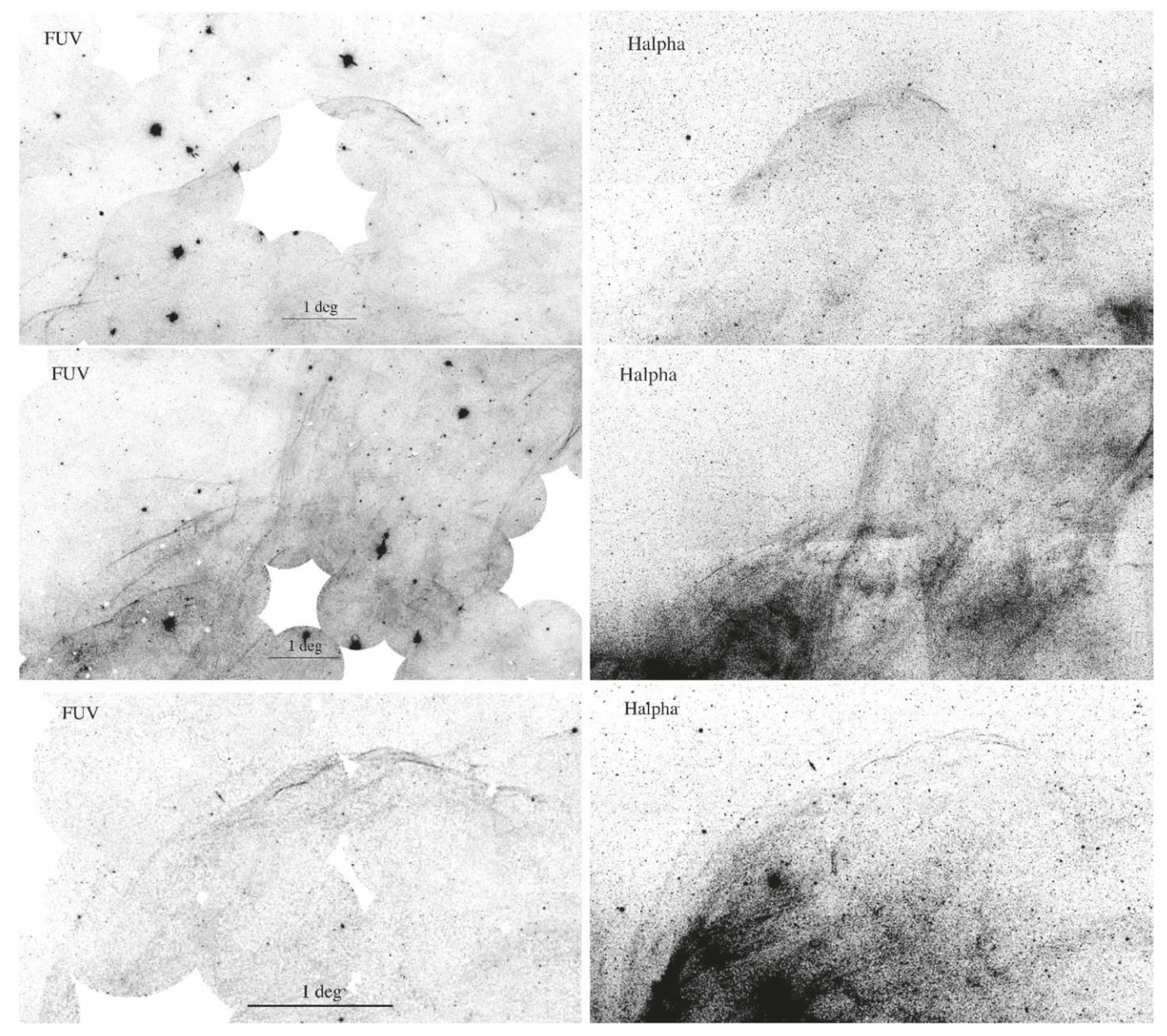


Figure 17. Comparison of GALEX FUV emission vs. MDW $H\alpha$ image mosaic of the northern, eastern, and southeastern portions of the Antlia SNR showing a close agreement of UV and $H\alpha$ emission filaments along its eastern boundary. There is considerable $H\alpha$ emission but little FUV emission in the nebula's interior. North is up, east to the left.

These optical spectra show clear evidence that the seven filaments observed distributed across the whole of the Antlia nebula exhibit line ratios indicative of shock emissions. In fact, emissions at Positions 4 and 6, located along Antlia's southeastern limb display nonradiative, pure Balmer line emission. Such shock spectra are usually seen in situations where the shock velocities are quite high (>500 km s⁻¹) as seen in young Type Ia SNRs like Tycho and SN 1006. However, similar Balmer-dominated spectra have also been seen in much older remnants (G107.+9.0; Fesen et al. 2020). Relatively slow shocks can remain nonradiative if the ambient density is sufficiently low, like that expected in the Galactic halo. This requires that the cooling time of the shocked gas

should be long enough to prevent the forbidden lines from becoming bright. Scaling the cooling times of Hartigan et al. (1987) with n_0^{-1} , the nonradiative shocks at the edge of a 100,000 yr old remnant in a density of $0.1 \, \mathrm{cm}^{-3}$ would be at least $170 \, \mathrm{km \, s}^{-1}$.

The other five filaments show optical spectra commonly seen in evolved SNRs like the Cygnus Loop and IC 443. In all these cases, the [S II]/H α ratio exceeds the 0.4 criterion for shock emission. Indeed, filaments 7 and 8 display ratios above 2, which are among the highest values observed in SNRs. Interestingly, these five filaments lack appreciable [O III] $\lambda\lambda4959,5007$ emission. Weak or absent [O III] emission indicates shock velocities less than about $70~{\rm km~s^{-1}}$. The high ${\rm H}\alpha/{\rm H}\beta$ ratio in Position 1 of the Antlia remnant suggests a substantial contribution of collisional excitation at fairly low temperatures to the Balmer lines, and this is borne out by the low [N II] and [S II] to H α ratios. That suggests shock

 $[\]overline{^{15}}$ Note: The [O I] emission seen in the spectrum for Position 4 is residual imperfect [O I] sky emission.

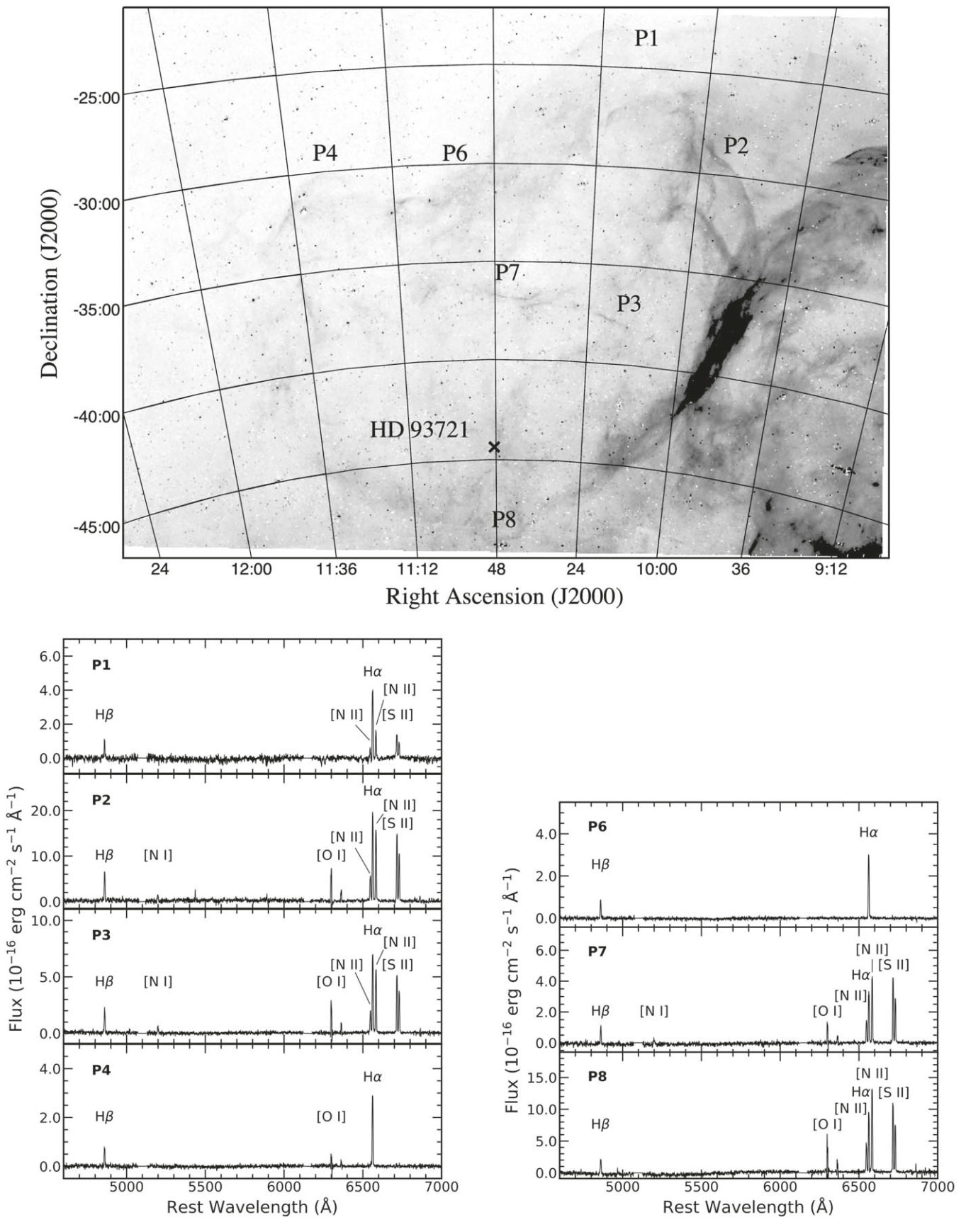


Figure 18. Top: continuum-subtracted SHASSA $H\alpha$ image mosaic of the Antlia remnant showing the locations of seven positions where SALT spectra were obtained. Bottom: observed optical spectra at these seven positions.

speeds around 70 km s⁻¹. Given these slow shock spectra along with pure Balmer emission spectra along the remnant's leading edges, there must be a considerable range of shock velocities present in the nebula. This is not too surprising given the large size of Antlia and a nearly 18° range in Galactic latitude.

4. Discussion

Based on the data presented above, we find that two suspected, high-latitude SNRs, namely G354–33 and Antlia, are likely bona fide SNRs. Moreover, their UV emission filaments appear best at marking these objects' forward shock front locations. Below we discuss supporting evidence for our conclusions, followed by estimates regarding their physical dimensions and general properties. We then briefly comment on the usefulness of far-UV imaging for SNR detection particularly in areas far off the Galactic plane.

4.1. G354.0-33.5

There are several observations that support the SNR identification of this large FUV, $H\alpha$, and radio emission nebula. At its Galactic latitude of $-33^{\circ}.5$, there are no bright and nearby early-type stars near the center of this UV shell that might have generated its UV emission shell through stellar winds. There is also no known nearby recurrent nova projected inside, and the emission shell is at least two orders of magnitude larger and does not have a similar appearance to known nova shells.

Then there is the large 1420 MHz radio emission shell roughly centered on and lying entirely within the borders of the FUV emission filaments. The FUV filaments also exhibit a shock-like morphology such as commonly seen in Galactic SNRs. Furthermore, its nearly continuous ring of thin filaments surrounds a broad, diffuse $H\alpha$ emission shell. In summary, its shock-like filamentary appearance and the positional agreement between UV, $H\alpha$, and radio emissions for such a large object located far off the Galactic plane leaves few viable options other than an SNR origin.

While we have not yet obtained optical spectra of its $H\alpha$ and UV filaments, based on the morphology of the ${\rm H}\alpha$ emission filament along its northwestern limb and the lack of [O III] emission, we suspect this remnant may resemble that of nonradiative filaments seen in a few remnants such as those that surround the northern and eastern limbs of the Cygnus Loop (Fesen et al. 1982; Raymond et al. 1983; Hester et al. 1994; Sankrit et al. 2000; Medina et al. 2014). A nonradiative or "Balmer-dominated" shock is one that heats plasma to a relatively high temperature and has encountered the plasma either so recently or is of such a low density that the gas has had insufficient time to radiatively cool and present optical line emissions. Such filaments are UV bright (Shull & McKee 1979; Raymond et al. 2003), a property consistent with GALEX FUV images for this object. Although the confirming test for the presence of nonradiative filaments in this remnant is spectra, the deep H α and [O III] images presented in Figure 6 support this conclusion.

Centered at a Galactic latitude around $-33^{\circ}.5$, G354–33 would rank as the highest Galactic latitude SNR found yet. In addition, if not for the Antlia remnant, this object would also have among the largest angular dimensions among the roughly 300 SNRs in the Green (2019) catalog. Because of its $\sim 11^{\circ} \times 14^{\circ}$ size and the fact that the largest known SNRs

have physical dimensions $\sim 100 \, \mathrm{pc}$, we can make some crude estimates of its distance and properties.

If its diameter is taken to be 100 pc, then its distance is around 400 pc. Based on the presence of its stronger FUV than NUV emission, its shock velocity is likely greater than 100 km s⁻¹ but probably less than 150 km s⁻¹, according to Figure 4 of Bracco et al. (2020). That shock speed is too high for this remnant to be in the snowplow phase of SNR evolution, but the presence of radiative shock waves around much of the rim indicates that it is no longer in the Sedov phase, at least in those places. That suggests that it is in the pressure-driven shell phase when the recently shocked gas has cooled, but there is still relatively hot, high-pressure gas in the interior.

From the calculations of Cioffi et al. (1988), this velocity range and a diameter of around 90 pc would be consistent with an age $\simeq 10^5$ yr and a preshock density of $0.1~\rm cm^{-3}$ (see Figure 14 of Fesen et al. 2020). One might expect detectable X-ray emission during the pressure-driven shell phase, but Shelton (1998) has discussed halo SNRs in which the interior gas is too cool to produce X-rays, but still rich in high-ionization states such as O VI.

4.2. G249.7+24.7

GALEX FUV, SHASSA, and MDM images show it displays a highly filamentary morphology like that commonly seen in SNRs. Moreover, optical spectra of its filaments reveal emission-line ratios consistent with the presence of shocks. The discovery of its X-ray emission along with associated radio emission and archival Parks radio data (Becker et al. 2021) leave little doubt that this object is a new SNR. With an angular dimension of 4°.5, the G249+24 remnant is among the largest of known SNRs. Situated at a Galactic latitude of over 24°, G249+24 also lies farther from the Milky Way's plane than any other confirmed SNR—that is, if it were not for G354–33.

The detection of high-velocity Na I absorptions in the spectrum of the star HD 83636, which has a Gaia EDR3 estimated distance of 386 pc, sets a maximum limit on G249+24's distance of less than 400 pc. This is less than the lower distance range of 400–500 pc estimated by Becker et al. (2021). If high-velocity Na I absorption lines are confirmed by subsequent higher-resolution echelle spectra, then the G249+24 remnant would then also rank among the closest SNRs known and with an especially robust distance limit.

The 400 pc upper limit on the distance implies an upper limit on its diameter of about 30 pc. It also provides an estimate of the ambient density. Fesen et al. (2020) used the separation between the sharp $H\alpha$ filaments of G107.0+9.0 and the diffuse [O III] emission to determine that remnant's preshock density. The angular separation between the $H\alpha$ and [O III] seen in Figure 13 is similar to that seen in G107.0+9.0, but here the distance upper limit is 2.5 times smaller than the 1 kpc distance adopted for G107.0+9.0. Therefore, the preshock density is at least 0.25 cm⁻³.

Because the emission from G249+24 is so faint, the density cannot be much higher than $0.25\,\mathrm{cm}^{-3}$, indicating that the distance is close to the upper limit. This is in accord with its morphology, which suggests that G247+24 is significantly above the Galactic disk and interacting with it on its southern side, indicating that it is more than $100\,\mathrm{pc}$ from the plane, and therefore more than $250\,\mathrm{pc}$ distant.

The pure Balmer line emission at P1 indicates that the remnant is still in the Sedov phase there, while the emission and absorption

spectra indicate shock speeds of ${\sim}60{-}100\,\mathrm{km\,s}^{-1}$ in most of the rest of the remnant. The faint X-ray emission and the 0.1 keV temperature found by Becker et al. (2021) also indicate that the remnant has left the Sedov phase and entered the pressure-driven shell phase. Assuming that the cooling occurred recently, when the shock speed fell below $400\,\mathrm{km\,s}^{-1}$, we can combine the Sedov equations for SNR radius and shock speed to estimate an age around 15,000 yr for a $10^{51}\,\mathrm{erg}$ explosion. Thus, the parameters of G247+24 are similar to those of the Cygnus Loop (Fesen et al. 2018) but is much fainter because it lacks the dense clouds that make parts of the Cygnus Loop bright at optical and X-ray wavelengths.

4.3. The Nature of the Antlia Nebula

McCullough et al. (2002) claimed this extraordinarily large emission nebula was a likely SNR based on its appearance in the deep $H\alpha$ image of the VTSS survey and on the presence of diffuse soft X-ray emission in its interior. However, this conclusion does not appear to be widely accepted, as measured by the remnant having attracted little subsequent attention.

This situation might in part be due to a reluctance by SNR researchers to accept its huge $20^{\circ} \times 26^{\circ}$ angular size, more than 3–5 times larger than the largest known confirmed SNRs, plus its location so close to the even larger 36° diameter Gum Nebula with its complex of large emission shells and wind-blown bubbles plus the embedded Vela SNR. Consequently, except for a far-UV study by Shinn et al. (2007) and a brief AAS abstract by Orchard et al. (2015), the Antlia remnant has not been studied in any detail, leaving open its properties and nature.

Our GALEX FUV mosaics show a well-defined shell in $H\alpha$ with many individual and overlapping filaments that strongly resemble ISM shocks. In addition, the locations of sharp UV filaments along the boundary of the object's $H\alpha$ emission are consistent with an SNR where such UV filaments mark the location of the remnant's shock front.

In addition, results of our seven optical spectra of Antlia's filaments clearly indicate shock emissions throughout the nebula and hence an SNR. These spectra include two textbook cases of nonradiative Balmer-dominated spectra (Positions 4 and 6), plus several other filaments exhibiting high [S II]/H α line ratios well above the 0.4 value distinguishing shocked from photoionized nebulae. We conclude that if the Antlia remnant was not so large, it would be an easy case for SNR classification.

If the FUV and optical images and spectra presented here were not enough to confirm the Antlia nebula as an SNR, the recently released eRosita All-Sky soft X-ray 0.3–2.3 keV image reveals a large emission shell at the site of the Antlia remnant (Predehl et al. 2020; Becker et al. 2021). Both the size and morphology of this X-ray-bright limb shell match those of the remnant's H α as shown in Figure 16. Although a full analysis of Antlia's X-ray emission properties is needed to assess its properties, the positional and morphological similarity of this X-ray shell to its FUV and H α emissions are strong additional indicators for an SNR classification.

The physical size of the Antlia SNR is uncertain due to its unknown distance. McCullough et al. (2002) estimated a wide range of possible distances, from 60 to 320 pc, and believed the remnant to be extremely old, at least 1 Myr, and hence in the final snowplow phase of SNR evolution. However, our optical spectra do not support such an old object or a distance less than 200 pc.

A 1 Myr old SNR is expected to have a a very low expansion velocity of around $10-20 \, \mathrm{km \, s^{-1}}$ (Chevalier 1977). In contrast, our optical spectra show line emissions indicating shock velocities between 50 and $150 \, \mathrm{km \, s^{-1}}$, making it a far younger ($<10^5 \, \mathrm{yr}$) remnant in the pressure-driven shell phase. Moreover, there are other data supporting a much younger remnant with relatively high-velocity gas inside.

Before the Antlia nebula was discovered, Bajaja et al. (1989) reported high-velocity clouds in the remnant's direction, with Penprase & Blades (1992) reporting high-velocity Ca II absorption lines in the spectrum of the B9/A0 III/IV star HD 93721, which lies in the direction of the Antlia SNR (see Figure 15). This star has an estimated Gaia Early Data Release 3 (EDR3) distance of 512 ± 7 pc. Penprase & Blades (1992) found at least 10 Ca II absorption components with $v_{\rm LSR}$ ranging from $-65~{\rm km~s}^{-1}$ to $+75~{\rm km~s}^{-1}$. Because a second star, HD 94724 ($d=210~{\rm pc}$), lying in the same general direction did not show any high-velocity components, they concluded that the high-velocity absorbing cloud's distance was between 200 and 500 pc. However, because not all stars behind an SNR display high-velocity absorption lines, a lack of high-velocity components does not provide a robust minimum distance estimate.

An alternative means of estimating the distance to the Antlia remnant is its apparent collision with the Gum Nebula (Gum 1952, 1955; Brandt et al. 1971; Sivan 1974; Chanot & Sivan 1983). Although the positional coincidence or abutment of the remnant's southwestern rim with the Gum Nebula's bright northeastern emission cloud has been noted in some studies of the Gum Nebula (Shinn et al. 2007; Iacobelli et al. 2014; Purcell et al. 2015), no proposal has been made about there being evidence for a physical interaction between the two nebulae.

Nonetheless, the SHASSA imaging of this region strongly indicates such a physical collision has occurred between the Antlia remnant and the Gum Nebula. The left panel of Figure 19 presents a section of the VTSS ${\rm H}\alpha$ image of the Galactic plane showing the Antlia emission shell, similar to the VTSS image presented in the McCullough et al. (2002) Antlia discovery paper. This shows Antlia's position relative to the Gum Nebula. The remnant's bright southern limb coincides with the northern rim of the Gum Nebula.

The right panel of Figure 19 shows a low-contrast version of our SHASSA image of Antlia. An unusual line of bright filaments nearly 10° in length can be seen in the projected overlap region of both shells (see also the top panel of Figure 18). The simplest explanation for such bright filaments situated only in the exact Antlia/Gum overlap region is that the Antlia remnant has collided with the outer northeastern rim of the Gum Nebula.

Support for an Antlia–Gum collision is shown in Figure 20 where wide-field $H\alpha$ (+N II]), [O III], and [S II] images are presented for the northern section of the Antlia–Gum Nebula overlap region. The left panel is a color-composite image revealing [O III] bright emission filaments out ahead of the [S II] bright emission filaments marking the location of a local shock front. The center panel highlights the much stronger [S II] emission filaments compared to the Gum Nebula's more diffuse emission. Because ISM shocks display stronger [S II] compared to that of $H\alpha$ as demonstrated in the Antlia spectra (see Table 4), the observed strong [S II] emission in the proposed collision filaments lends support for a collision scenario. This conclusion is further indicated by the right panel, which shows the observed ratio of $F([S II])/F(H\alpha + [N II])$ with the stars removed. The sharp dark filaments in this panel

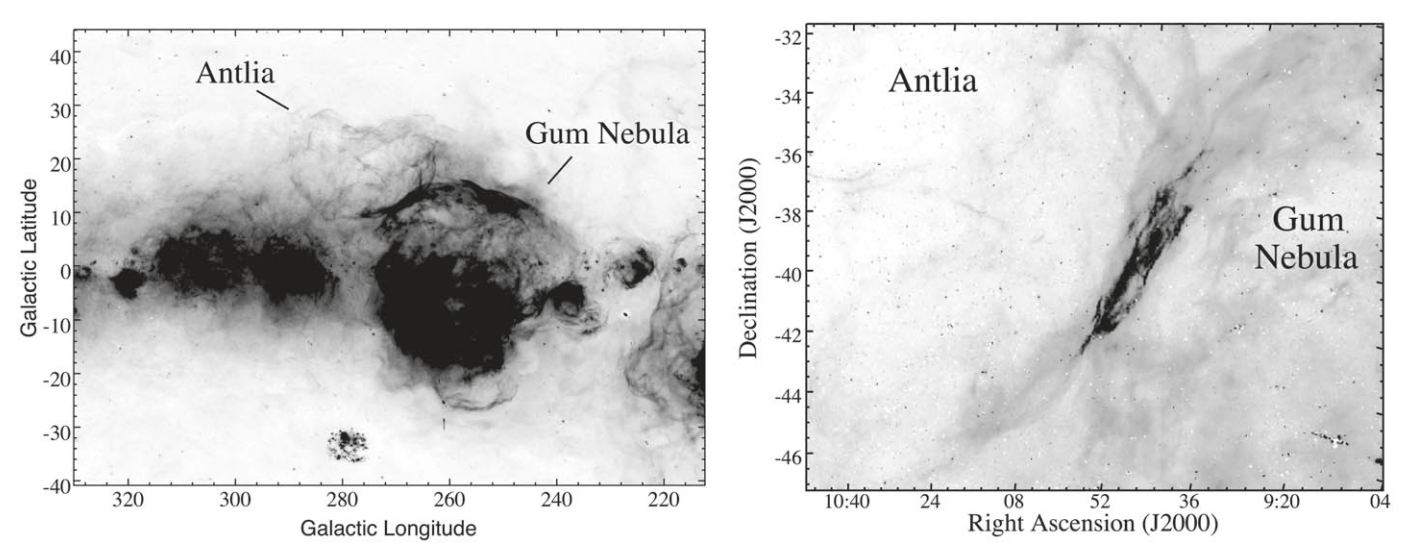


Figure 19. Left: VTSS $H\alpha$ image of the Galactic plane around the Gum Nebula with the location of the Antlia SNR marked. Right: the continuum-subtracted SHASSA $H\alpha$ image of the Antlia remnant showing the presence of bright filaments at the overlapping Antlia and Gum Nebula region suggestive of a physical interaction.

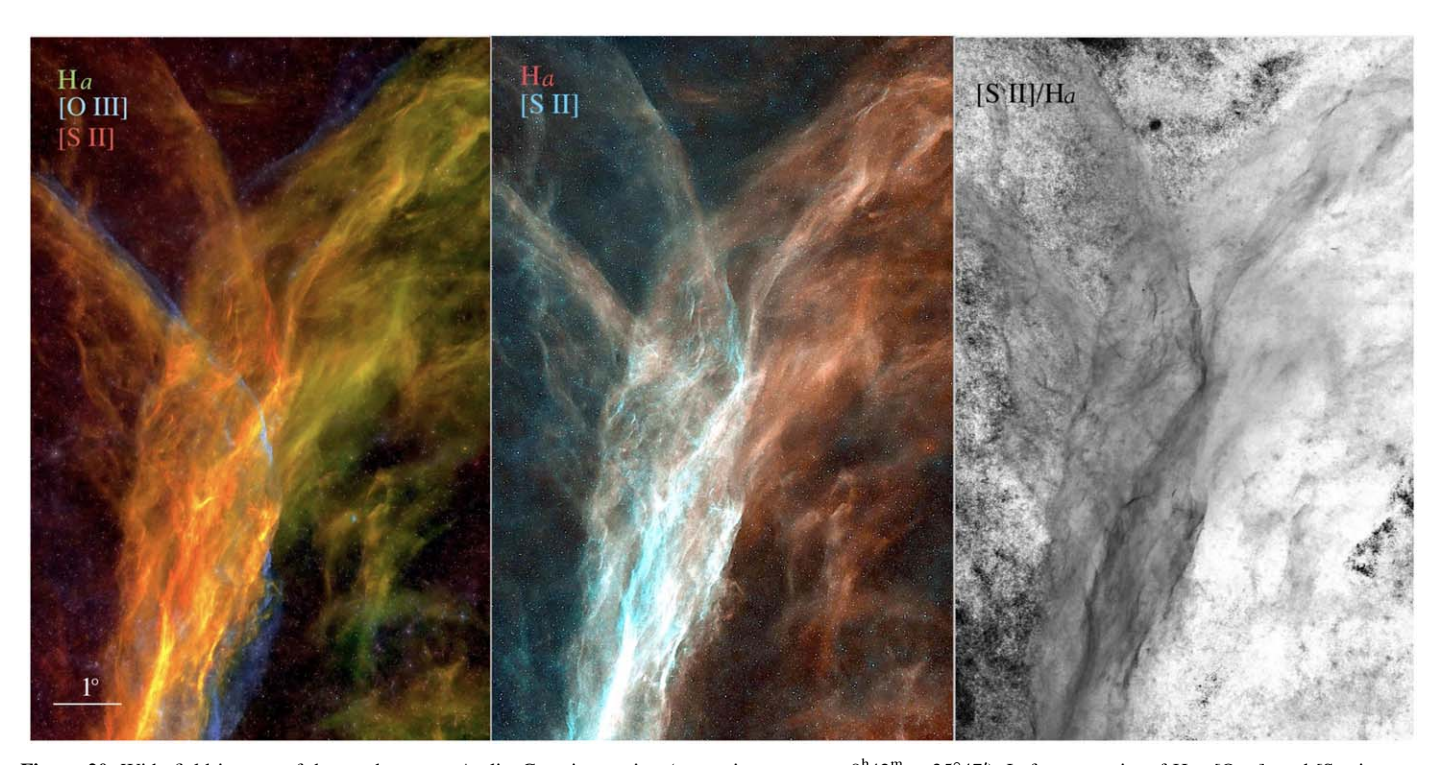


Figure 20. Wide-field images of the northwestern Antlia–Gum interaction (approximate center: $9^{h}42^{m}$, $-35^{\circ}47'$). Left: composite of H α , [O III], and [S II images. Center: composite of H α and [S II images. Right: ratio of H α and [S II images.

image represent ratios between 1 and 1.3, values consistent with the measured spectral line strengths of Antlia's shock filaments (see Table 4).

If the Antlia remnant's expansion has led to a collision of it with an outer portion of the Gum Nebula, then the Antlia's distance must be roughly the same as for the Gum Nebula. Unfortunately, the distance to the Gum Nebula is poorly known, with values ranging from 200 to 500 pc (Brandt et al. 1971; Zealey et al. 1983; Graham 1986; Woermann et al. 2001; Kim et al. 2005; Howarth & van Leeuwen 2019). Nonetheless, distances much below 200 pc like those suggested by McCullough et al. (2002) would appear to

be ruled out, as would the suggestion by Tetzlaff et al. (2013) that the 1.2 Myr old PSR J0630–2834 was formed in the Antlia remnant at a distance \approx 135 pc.

If we adopt recent distance estimates to the Gum of $300{\text -}450\,\mathrm{pc}$, which include estimates for some of the Gum Nebula's ionizing stars (ζ Pup; Howarth & van Leeuwen 2019), then the Antlia remnant's physical diameter is $\sim 120{\text -}180\,\mathrm{pc}$. However, given the Gum Nebula's 36° diameter, its outer parts extend over a distance of some $200{\text -}300\,\mathrm{pc}$ along the line of sight, and this greatly complicates using a collision scenario to constrain the Antlia remnant's distance.

Table 4Observed Emission-line Fluxes for Antlia Filaments

Emission Line		Filament Position								
(Å)	P1	P2	Р3	P4	P6	P7	P8			
Hβ 4861	100	100	100	100	100	100	100			
[O III] 5007	<10	< 10	<10	<10	<10	<10	<10			
[N I] 5200		23	29			20				
[O I] 6300		93	98			101	122			
[N II] 6548	57	89	97			137	181			
$H\alpha$ 6563	430	300	339	379	368	304	365			
[N II] 6583	167	247	275			403	542			
[S II] 6716	146	239	247			406	442			
[S II] 6731	91	167	184			283	307			
$F([S II])/F(H\alpha)$	0.55	1.35	1.27			2.27	2.05			
[S II] 6716/6731	1.60	1.43	1.34			1.43	1.44			
E(B-V)	0.35	0.00	0.12	0.23	0.20	0.01	0.19			
$F(H\alpha) \text{ erg cm}^{-2} \text{ s}^{-1}$	2.74E-15	1.29E-14	4.75E-15	1.91E-15	2.06E-15	2.16E-15	6.06E-15			

4.4. The Power of FUV Emissions for Finding Interstellar Shocks

A few large Galactic SNRs and superbubbles have been recently studied in terms of their far-UV emissions. For example, studies of far-UV emissions have been reported for the Vela SNR (Nishikida et al. 2006), the Cygnus Loop (Seon et al. 2006), the Lupus Loop (Shinn et al. 2006), and the Orion–Eridanus Superbubble (Kregenow et al. 2006). Many of these made use of the SPEAR imaging spectrograph (Edelstein et al. 2006).

However, there have been few papers reporting discoveries of large interstellar emission structures using FUV emissions. One such paper is that of Bracco et al. (2020), who reported finding a 30° long UV arc in Ursa Major using GALEX images. That work was a follow-up to an earlier detection of a much shorter 2°.5 filament by McCullough & Benjamin (2001) using deep $H\alpha$ imaging. However, only through the GALEX's FUV images was the full extent of this faint, long interstellar filament finally revealed.

The FUV emission of moderate-velocity shocks is dominated by the hydrogen two-photon continuum, resonance lines of C IV and Mg II, and intercombination lines such as C III] and Si III]. Bracco et al. (2020) computed the GALEX FUV and NUV count rates for shocks from the Sutherland & Dopita (2017) MAPPINGS models. Shocks slower than about 100 km s^{-1} are dominated by the two-photon continuum, while faster shocks have strong contributions from C IV and other lines. The predicted ratios range from about 0.1 to 0.9. Based on our own model calculations, a reddening $E(B-V) \sim 0.1$ does not affect the ratios very much, though it reduces both the NUV and FUV count rates by a factor of 2. A major caveat, however, is that scattering in edge-on sheets of emitting gas, in particular SNR filaments, can strongly reduce the intensities of resonance lines such as C IV (Cornett et al. 1992), reducing the FUV/NUV ratio.

Above we have presented large GALEX FUV mosaic images of two large nebulae, which appear to be true Galactic SNRs but were either only suspected or missed in most radio studies that have concentrated their searches near the Galactic plane. The object G249+24 also appears to have been missed in wide FOV optical surveys due to its relatively weak ${\rm H}\alpha$ emissions.

Both our investigations and that of Bracco et al. (2020) indicate that broad, far-UV imaging can be an especially useful means for detecting and distinguishing interstellar shocks and, in some cases, is more sensitive compared to $H\alpha$ imaging. As

noted by Bracco et al. (2020), both line emissions and two-photon continuum emissions contribute to FUV emission in shocks with velocities above $\simeq 50 \, \mathrm{km \, s}^{-1}$.

To illustrate the usefulness of far-UV emission imaging for detecting SNRs, Bracco et al. (2020) noted the presence of networks of thin FUV filaments in both the Antlia SNR and the recently discovered Galactic remnant G70.0-21.5 (Boumis et al. 2002; Fesen et al. 2015; Raymond et al. 2020). In Figure 21 we show a comparison of MDW's H α image and the GALEX FUV image of G70.0-21.5. Until the study of the SNRs discussed here, this remnant at $b = -21^{\circ}.5$ had been the remnant with the highest Galactic latitude. This figure nicely demonstrates how the FUV image makes the remnant easy to detect and helps to define its full dimensions despite the many missing individual GALEX images. Knowing about the existence of these GALEX FUV images could have helped Fesen et al. (2015) and Raymond et al. (2020) in their analyses of this remnant with regard to the remnant's true physical size. In summary, therefore, far-UV images appear to be an especially useful tool for identifying interstellar shocks like those found in SNRs, albeit best suited for high Galactic latitude searches.

5. Conclusions

We have investigated the nature of two large and suspected SNRs located at unusually high Galactic latitudes through GALEX far-UV emission mosaics and optical images and spectra. This research has also uncovered one new Galactic SNR. Our findings include:

- 1. The large radio emission shell, G354.0–33.5, seen in 1420 MHz and 1.4 GHz radio polarization maps is very likely an SNR. The remnant exhibits numerous sharp FUV emission filaments in a thin, unbroken shell with angular dimensions of $11^{\circ} \times 14^{\circ}$.0. It also exhibits a coincident H α emission shell.
- 2. A group of bright, sharp FUV emission filaments coincident with numerous but faint $H\alpha$ filaments appears to be a previously unrecognized SNR, G249.7+24.7. Optical spectra of several filaments show evidence for the presence of 50–150 km s⁻¹ shocks. Deep $H\alpha$ images reveal a highly filamentary morphology like that seen in evolved SNRs. Becker et al. (2021) independently discovered this remnant as a circular 4.4° shell of diffuse,

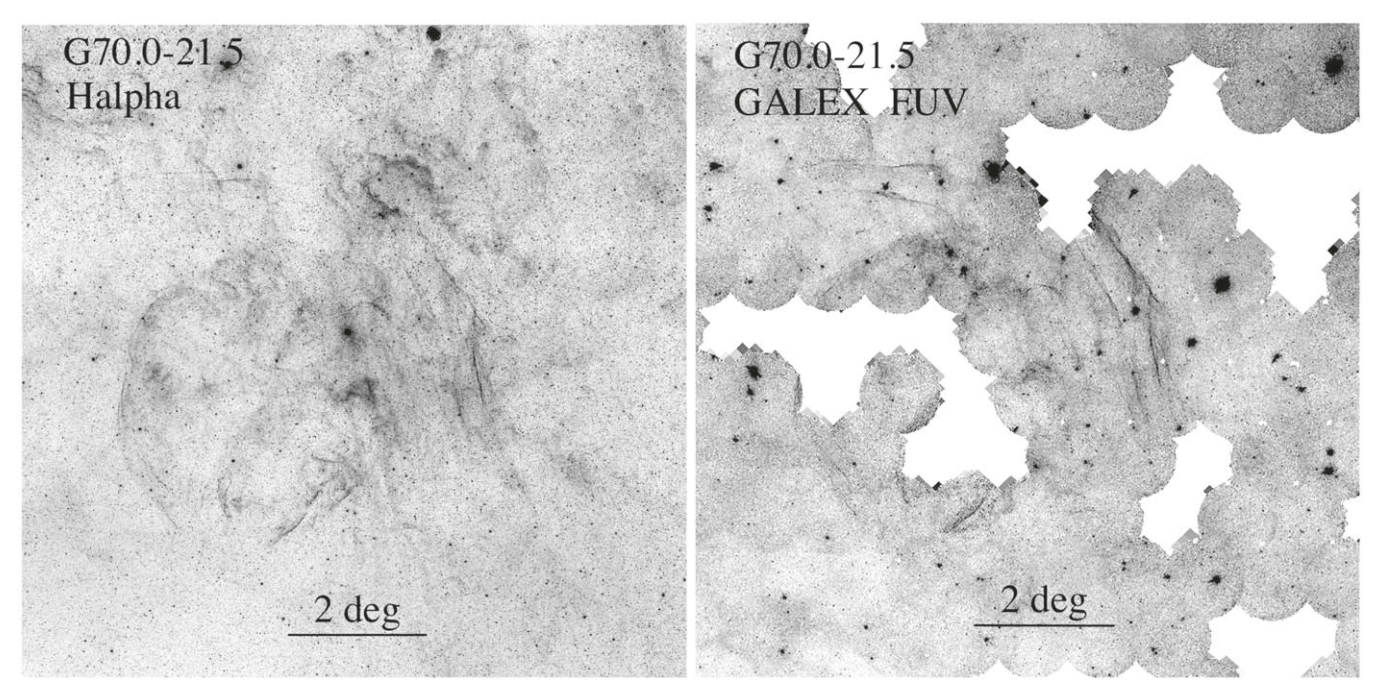


Figure 21. Comparison of the MDW H α and GALEX FUV images of the high-latitude remnant G70.0-21.5. North is up, east to the left.

soft X-ray emission (0.1 keV) with an estimated radio spectral index of -0.69 ± 0.08 . Moderate-dispersion optical spectra of two stars lying in the direction of this remnant have been found to exhibit high-velocity, redand blueshifted Na I absorption lines in the range of $55-73~\rm km~s^{-1}$, with one star showing an added blue absorption feature at $-125~\rm km~s^{-1}$. The closest of these two stars lies at a Gaia-estimated distance of 386 pc, which, if confirmed by follow-up higher dispersion data, sets a strict maximum distance to the G249.7+24.7 SNR at less than 400 pc, making it one of the closest Galactic SNRs known.

- 3. Despite its enormous angular dimensions $(20^{\circ} \times 26^{\circ})$, our GALEX FUV mosaic images, plus wide-angle $H\alpha$ images and optical spectra strongly support an SNR origin for the Antlia nebula. This conclusion is in line with a reported $\pm 70\,\mathrm{km\,s^{-1}}$ Ca II absorption in one background star. We estimate an age of $\sim \! 10^5\,\mathrm{yr}$, which is an order of magnitude less than the earlier estimate $\sim \! 1\,\mathrm{Myr}$. We also find the remnant is likely in direct physical contact along its southwestern rim with the Gum Nebula
- 4. Our investigation of suspected SNRs located at unusually high Galactic latitudes (>15°) highlights the value of UV images to detect interstellar shocks.

Follow-up work on these three objects could include optical spectra of the FUV and $H\alpha$ filaments of the G354–33 remnant, wide-field [O III] $\lambda5007$ imaging of G249+24 exploring its [O III] emission, and high-dispersion echelle spectra of the two apparent background stars toward G249+24 to investigate our reported high-velocity Na I absorption lines. Higher-resolution $H\alpha$ images and optical spectra of the series of long and very bright filaments seen in the southwestern limb of the Antlia remnant could also provide an additional test of our conclusion regarding Antlia's collision with the Gum Nebula.

Although we have found that all three nebulae in our study are SNRs, only the G249.7+24.7 remnant has a distance or upper limit estimate, leaving us with only approximate physical parameters and evolutionary status. This problem can be addressed especially well for the other two objects, G354.0-33.5 and Antlia, given their enormous angular dimensions and hence offering numerous potential background stars to explore high-velocity ISM absorptions. Given the era of accurate Gaia parallaxes, obtaining highdispersion spectra looking for high-velocity Na I $\lambda\lambda$ 5890,5896 and Ca II $\lambda 3934$ absorptions in background stars like that done for several SNRs could be quite fruitful (e.g., Vela: Jenkins et al. 1976; Danks & Sembach 1995; Cha & Sembach 2000; IC 443: Welsh & Sallmen 2003; S147: Sallmen & Welsh 2004; Cygnus Loop: Fesen et al. 2018; W28: Ritchey 2020). Such observations might also help gauge the range of shock velocities across the very large and expansive remnants of G354.0-33.5 and Antlia.

Our findings that both the G354.0–33.5 and Antlia nebula are real SNRs were a bit of a surprise. Out of the 300 or so confirmed SNRs, there are only about a dozen SNRs larger than 2° and less than half that number located more than 10° off the Galactic plane (Green 2015, 2019). Now with the realization that some Galactic remnants can reach angular sizes several times larger than even Vela, it encourages the investigation of other large emission shells suspected as possible SNRs or previously viewed as unlikely SNR candidates. It also raises the value of SNR searches in the $|b| > 10^{\circ}$ range, generally viewed before as unproductive.

Finally, we note that although far-UV imaging appears to be a sensitive new tool for uncovering the presence of interstellar shocks, it is most useful in searching uncomplicated regions, like the objects discussed here located in the Galactic halo. However, the number of similar but unrecognized high-latitude Galactic remnants is probably pretty small. Nonetheless, given the dozens of unconfirmed but seemingly likely or suspected SNRs in the literature (see the list in Green's 2019 catalog), many new SNR discoveries may be aided by the use of UV imaging.

We thank Eric Galayda and the entire MDM staff for making the optical observations possible, and the SALT Observatory and Resident Astronomer staff for obtaining the excellent RSS spectra despite disruptions due to COVID-19 restrictions. We also thank R. Benjamin for helpful discussions. This work made use of the Simbad database, NASA's Skyview online data archives, and the Max Planck Institute for Radio Astronomy Survey Sampler. This work is part of R.A.F's Archangel III Research Program at Dartmouth. D.M. acknowledges support from the National Science Foundation from grants PHY-1914448 and AST-2037297.

Note Added in Proof: New high-dispersion SALT HRS echelle spectra of nearly two dozen stars located towards the G354-33 SNR revealed 50–80 km/s velocity Na I or Ca II absorption lines in four stars which lead to a new distance estimate <275 pc, less than the 400 pc value discussed in the paper.

ORCID iDs

```
Robert A. Fesen https://orcid.org/0000-0003-3829-2056
Kathryn E. Weil https://orcid.org/0000-0002-8360-0831
John C. Raymond https://orcid.org/0000-0002-7868-1622
Dan Milisavljevic https://orcid.org/0000-0002-0763-3885
Bhagya M. Subrayan https://orcid.org/0000-0001-8073-8731
```

Dennis di Cicco https://orcid.org/0000-0003-1235-7173 Sean Walker https://orcid.org/0000-0003-2692-2321

References

```
Alikakos, J., Boumis, P., Christopoulou, P. E., & Goudis, C. D. 2012, A&A,
   544, A140
Aschenbach, B. 1998, Natur, 396, 141
Bajaja, E., Cappa de Nicolau, C. E., Martin, M. C., et al. 1989, A&AS, 78, 345
Becker, W., Hurley-Walker, N., Weinberger, C., et al. 2021, A&A, 648, A30
Bianchi, L. 2009, Ap&SS, 320, 11
Blair, W. P., Kirshner, R. P., & Chevalier, R. A. 1981, ApJ, 247, 879
Blondin, J. M., Wright, E. B., Borkowski, K. J., & Reynolds, S. P. 1998, ApJ,
   500, 342
Boumis, P., Mavromatakis, F., Paleologou, E. V., & Becker, W. 2002, A&A,
   396, 225
Boumis, P., Xilouris, E. M., Alikakos, J., et al. 2009, A&A, 499, 789
Bracco, A., Benjamin, R. A., Alves, M. I. R., et al. 2020, A&A, 636, L8
Brandt, J. C., Roosen, R. G., Thompson, J., & Ludden, D. J. 1976, ApJ,
Brandt, J. C., Stecher, T. P., Crawford, D. L., & Maran, S. P. 1971, ApJL,
Cha, A. N., & Sembach, K. R. 2000, ApJS, 126, 399
Chanot, A., & Sivan, J. P. 1983, A&A, 121, 19
Chevalier, R. A. 1977, ARA&A, 15, 175
Cioffi, D. F., McKee, C. F., & Bertschinger, E. 1988, ApJ, 334, 252
Condon, J. J., Cotton, W. D., Greisen, E. W., et al. 1998, AJ, 115, 1693
Cornett, R. H., Jenkins, E. B., Bohlin, R. C., et al. 1992, ApJL, 395, L9
Cox, D. P., & Smith, B. W. 1974, ApJL, 189, L105
Danks, A. C., & Sembach, K. R. 1995, AJ, 109, 2627
Dopita, M. A., Binette, L., Dodorico, S., & Benvenuti, P. 1984, ApJ, 276,
Downes, D. 1971, AJ, 76, 305
Driessen, L. N., Domček, V., Vink, J., et al. 2018, ApJ, 860, 133
Edelstein, J., Korpela, E. J., Adolfo, J., et al. 2006, ApJL, 644, L159
Ferrand, G., & Safi-Harb, S. 2012, AdSpR, 49, 1313
Fesen, R. A., Blair, W. P., & Kirshner, R. P. 1982, ApJ, 262, 171
Fesen, R. A., Blair, W. P., & Kirshner, R. P. 1985, ApJ, 292, 29
Fesen, R. A., Neustadt, J. M. M., Black, C. S., & Koeppel, A. H. D. 2015, ApJ,
Fesen, R. A., Neustadt, J. M. M., How, T. G., & Black, C. S. 2019, MNRAS,
Fesen, R. A., Weil, K. E., Cisneros, I. A., Blair, W. P., & Raymond, J. C. 2018,
   MNRAS, 481, 1786
```

```
Finkbeiner, D. P. 2003, ApJS, 146, 407
Gaustad, J. E., McCullough, P. R., Rosing, W., & Van Buren, D. 2001, PASP,
  113, 1326
Graham, J. A. 1986, ApJ, 302, 352
Green, D. A. 1984, MNRAS, 209, 449
Green, D. A. 2004, BASI, 32, 335
Green, D. A. 2015, MNRAS, 454, 1517
Green, D. A. 2019, JApA, 40, 36
Gum, C. S. 1952, Obs, 72, 151
Gum, C. S. 1955, MmRAS, 67, 155
Hartigan, P., Raymond, J., & Hartmann, L. 1987, ApJ, 316, 323
Haslam, C. G. T., Klein, U., Salter, C. J., et al. 1981, A&A, 100, 209
Haslam, C. G. T., Salter, C. J., Stoffel, H., & Wilson, W. E. 1982, A&AS, 47, 1
Hester, J. J., Raymond, J. C., & Blair, W. P. 1994, ApJ, 420, 721
How, T. G., Fesen, R. A., Neustadt, J. M. M., Black, C. S., & Outters, N. 2018,
   MNRAS, 478, 1987
Howarth, I. D., & van Leeuwen, F. 2019, MNRAS, 484, 5350
Howell, D. A. 2017, in Superluminous Supernovae, ed. A. W. Alsabti &
  P. Murdin (Cham: Springer International Publishing AG), 431
Iacobelli, M., Burkhart, B., Haverkorn, M., et al. 2014, A&A, 566, A5
Jenkins, E. B., Silk, J., & Wallerstein, G. 1976, ApJS, 32, 681
Kim, J. S., Walter, F. M., & Wolk, S. J. 2005, AJ, 129, 1564
Kopsacheili, M., Zezas, A., & Leonidaki, I. 2020, MNRAS, 491, 889
Kregenow, J., Edelstein, J., Korpela, E. J., et al. 2006, ApJL, 644, L167
Leonidaki, I., Boumis, P., & Zezas, A. 2013, MNRAS, 429, 189
Long, K. S. 2017, in Galactic and Extragalactic Samples of Supernova
  Remnants: How They Are Identified and What They Tell Us, ed.
  A. W. Alsabti & P. Murdin (Cham: Springer International Publishing
  AG) 2005
Maggi, P., Haberl, F., Kavanagh, P. J., et al. 2014, A&A, 561, A76
Martini, P., Stoll, R., Derwent, M. A., et al. 2011, PASP, 123, 187
Massey, P., & Gronwall, C. 1990, ApJ, 358, 344
McCullough, P. R., & Benjamin, R. A. 2001, AJ, 122, 1500
McCullough, P. R., Fields, B. D., & Pavlidou, V. 2002, ApJL, 576, L41
McKee, C. F., & Ostriker, J. P. 1977, ApJ, 218, 148
Medina, A. A., Raymond, J. C., Edgar, R. J., et al. 2014, ApJ, 791, 30
Morrissey, P., Conrow, T., Barlow, T. A., et al. 2007, ApJS, 173, 682
Neustadt, J. M. M., Fesen, R. A., & Black, C. S. 2017, MNRAS, 469, 516
Nishikida, K., Edelstein, J., Korpela, E. J., et al. 2006, ApJL, 644, L171
Oke, J. B. 1974, ApJS, 27, 21
Orchard, A., Benjamin, R. A., Gostisha, M., et al. 2015, AAS Meeting
  Abstracts, 225, 140.44
Osterbrock, D. E., & Ferland, G. J. 2006, Astrophysics of Gaseous Nebulae
  and Active Galactic Nuclei (Sausalito, CA: University Science Books)
Penprase, B. E., & Blades, J. C. 1992, ApJ, 391, 276
Pfeffermann, E., & Aschenbach, B. 1996, in International Conference on X-ray
   Astronomy and Astrophysics: Röntgenstrahlung from the Universe, ed.
  H. U. Zimmermann, J. Trümper, & H. Yorke, 267
Predehl, P., Sunyaev, R. A., Becker, W., et al. 2020, Natur, 588, 227
Purcell, C. R., Gaensler, B. M., Sun, X. H., et al. 2015, ApJ, 804, 22
Raymond, J. C., Blair, W. P., Fesen, R. A., & Gull, T. R. 1983, ApJ, 275, 636
Raymond, J. C., Caldwell, N., Fesen, R. A., et al. 2020, ApJ, 888, 90
Raymond, J. C., Ghavamian, P., Sankrit, R., Blair, W. P., & Curiel, S. 2003,
    pJ, 584, 770
Reich, W. 1982, A&AS, 48, 219
Reich, W., & Reich, P. 2009, in Cosmic Magnetic Fields: From Planets, to
  Stars and Galaxies, IAU Symposium, 259, ed. K. G. Strassmeier,
   A. G. Kosovichev, & J. E. Beckman (New York: Cambridge Univ.
  Press), 603
Ritchey, A. M. 2020, MNRAS, 495, 2909
Sabin, L., Parker, Q. A., Contreras, M. E., et al. 2013, MNRAS, 431, 279
Sallmen, S., & Welsh, B. Y. 2004, A&A, 426, 555
Sankrit, R., Blair, W. P., Raymond, J. C., & Long, K. S. 2000, AJ, 120, 1925
Seon, K. I., Han, W., Nam, U. W., et al. 2006, ApJL, 644, L175
Shelton, R. L. 1998, ApJ, 504, 785
Shinn, J. H., Min, K. W., Lee, C. N., et al. 2006, ApJL, 644, L189
Shinn, J.-H., Min, K. W., Sankrit, R., et al. 2007, ApJ, 670, 1132
Shull, J. M., Fesen, R. A., & Saken, J. M. 1989, ApJ, 346, 860
Shull, J. M., & McKee, C. F. 1979, ApJ, 227, 131
Sivan, J. P. 1974, A&AS, 16, 163
Stupar, M., & Parker, Q. A. 2011, MNRAS, 414, 2282
Stupar, M., & Parker, Q. A. 2012, MNRAS, 419, 1413
Stupar, M., Parker, Q. A., Filipović, M. D., et al. 2007, MNRAS, 381, 377
Stupar, M., Parker, Q. A., & Filipović, M. D. 2008, MNRAS, 390, 1037
Stupar, M., Parker, Q. A., & Frew, D. J. 2018, MNRAS, 479, 4432
```

Fesen, R. A., Weil, K. E., Raymond, J. C., et al. 2020, MNRAS, 498, 5194

Sutherland, R. S., & Dopita, M. A. 2017, ApJS, 229, 34
Testori, J. C., Reich, P., Bava, J. A., et al. 2001, A&A, 368, 1123
Testori, J. C., Reich, P., & Reich, W. 2008, A&A, 484, 733
Tetzlaff, N., Torres, G., Neuhäuser, R., & Hohle, M. M. 2013, MNRAS, 435, 879

van Dokkum, P. G. 2001, PASP, 113, 1420
Welsh, B. Y., & Sallmen, S. 2003, A&A, 408, 545
Woermann, B., Gaylard, M. J., & Otrupcek, R. 2001, MNRAS, 325, 1213
Zealey, W. J., Ninkov, Z., Rice, E., Hartley, M., & Tritton, S. B. 1983, Astrophys. Lett., 23, 119